NANOSTRUCTURING OF CU-TIB_2 INDUCED BY ION IRRADIATION

BY

RANNESH LOKESH

THESIS

Submitted in partial fulfillment of the requirements
for the degree of Master of Science in Materials Science and Engineering
in the Graduate College of the
University of Illinois at Urbana-Champaign, 2011

Urbana, Illinois

Advisers:

Professor Pascal Bellon
Professor Robert S Averback

ABSTRACT

The stability of materials under irradiation is a critical topic and has been an area of fundamental interest in particular for materials used in nuclear reactors. These dissipative systems which exist far from equilibrium pose a challenge in understanding due to the existence of multiple dynamical processes, which are often competing. Recent modeling and experimental results of Cu-base alloys indicate that these dynamical processes can lead to nanostructuring in binary alloy system. Nanostructuring at steady state under irradiation could result in materials with very high irradiation resistance as interfaces can trap point defects and He atoms. The objective of this work was to study whether nanostructuring could also take place in multicomponent systems, possible involving the precipitation of compounds. The Cu-TiB_2 alloy system was selected and microstructural evolutions induced by 1.8 MeV Kr ion irradiation with varying fluence and wide range of temperatures were investigated. An additional objective was to identify the mode of formation of these nanostructures. Homogeneous co-sputtered Cu-TiB_2 films as well as Cu/TiB_2 multilayers were grown by physical vapor deposition as starting materials. Transmission electron microscopy revealed that irradiation of initially homogeneous films led to the nanoscale precipitation of second phase TiB_2 particles, with an average diameter of 5 nm. This nanostructuring reached similar steady states for irradiation temperatures ranging from room temperature to 650 °C. It is thus concluded that this nanoprecipitation takes place in displacement cascades.

Keywords: Copper alloys, nanostructure, transmission electron microscopy, precipitation

ACKNOWLEDGEMENTS

It's been a strange and interesting journey over the past 3 years and there are so many people involved and I would like to take this opportunity to thank them all.

Firstly, I would like to thank my adviser Prof. Pascal Bellon who has been a great support and without whom this thesis would not be possible. His guidance and constant motivation throughout the project was invaluable. His words of encouragement in difficult times as a mentor and his kind nature are things I cannot forget. Thank you, Pascal.

I would also like to thank Prof. Robert Averback for his straightforward comments and ideas in the project. His experience, knowledge and brilliance have helped me a lot and I have learnt a lot from you. Thank you, Bob.

This work would never have been if not for the love and support of my parents. Thanks for letting me pursue my dreams and having stood by my side at all times. Ma and Appa, thank you. And of course, my lovely little sister, Vydu whom I missed the most.

I would like also like to take this opportunity to thank the staff of Center of Microanalysis of Materials, without whose guidance and training any of this would have been possible. They have been very kind enough sharing their knowledge and spending hours together with me. To the research staff, who trained me on different instruments, Mr. Doug Jeffers, Dr. Jian-Guo Wen, Dr. Wacek Swiech, Dr. Changhui Lei, Dr. Mauro Sardela, Mr. Mike Marshall, Dr. Jim Mabon, Dr. Scott Maclaren, Dr. Rick Haasch, Mr. Steve Burdin, Mr. Ernie Sammann, Dr. Vania Petrova. It was a pleasure working with you all.

I wish to thank the present and past group members of Bob and Pascal. Brad, Elvan, Tim, Vo, Xuan, Kai Ping, Daniel, Yinon, Miao, Shipeng, Wenjun, Wai and Anoop. It was fun working with you all over the past three years and I wish you all, the best for the future.

This would be incomplete if not for the mention of my friends in Chambana. I cannot imagine my life here without you guys. Thank you, Adi, Som, Abhishek, Prannoy, Laavi, Sneha, Aashana, Sravanthi, Varun, Sangeetha, Murthy, Preeti, Jayanta.

Thanks are also due to my other school friends who have been a constant support to me indirectly. Thanks Rama, Jesu, JB, Rohit, Avi, Kunal, Chethan & Rajatha.

I gratefully acknowledge the funding source for this project. This research was supported by the NSF under the grant DRM 08-04615. This work was carried out in part in the Frederick Seitz Materials Research Laboratory Central Facilities, University of Illinois, which are partially supported by the U. S. Department of Energy under the grants DE-FG02-07ER46453 and DE-FG02-07ER46471. I would also like to thank Department of Materials Science and Engineering for offering me Teaching Assistantships for the last year helping me with the funding.

TABLE OF CONTENTS

CHAPTER 1

INTRODUCTION

The effects of radiation on the properties of solids are of significant interest in both scientific and technological fields primarily due to their importance for applications such as nuclear reactors and ion beam processing of materials. Major effects of radiation on solids were observed after nuclear fission reactors were developed in the 1940s and since then study of the structural effects of radiation in materials has gained significant technological importance. Radiation can also bring about changes in composition of the material either by ion implantation or by transmutation, and in recent years it has become a major technique in the manufacture of silicon devices [1]. Particle irradiation remains a powerful tool to study the underlying properties of point defects, and irradiation with energetic heavy ions drives the system far from equilibrium providing newer perspective to study and understand the properties of these dissipative materials [2]. As a non equilibrium process, ion beam irradiation is instrumental in phase transformation and material modification in solids [3].

It is very important to understand and control chemical and physical phenomena in complex systems at high temperatures and radiation doses. A clear understanding of microstructural evolution and subsequent property variation under extreme conditions is critical for design of structural materials, fuels and waste-form applications [4]. The microstructure development under irradiation is primarily governed by the motion of point defects and the atomic mixing of the alloy constituents [5]. In immiscible alloy systems, a competition may arise between the thermally activated motion of the point defects and solute fluxes which lead to de-mixing, with atomic mixing due to ballistic collision cascade and liquid like mixing in the thermal spike region in the cascade. Martin

[6] in 1984 introduced a model to account for the dynamical competition between thermally activated decomposition and ballistic mixing. Martin showed that the steady state reached by such a system is identical to the equilibrium state that would have been reached at a higher, effective temperature, which is defined by $T_{eff} = T\,(1 + \frac{D(ballistic)}{D(th)})$. At high fluxes and low temperature, the alloy system is predicted to form a solid solution whereas at relatively high temperatures and low flux, the system becomes phase separated. In Martin's model, the ballistic mixing is assumed to be short ranged, and is thus modeled as a forced diffusive process. Molecular dynamics simulations have however revealed that the distribution of atomic relocations in displacement cascades can exhibit a tail that contains relocations to several nearest neighbor distances [7]. Enrique and Bellon introduced a new model to take into account that finite range mixing. Analytical modeling and kinetic Monte Carlo simulations indicated that, owing to the finite-range mixing, in addition to a solid solution and macroscopically decomposed state, a third steady state was possible consisting of self organized structures with nanometer length scale [8]. Such nanostructures have been experimentally observed in alloy systems such as Cu-Co [9], Cu-Ag and Cu-Fe [10]. In addition to fundamental interest, steady state self organized nanostructures are interesting for applications requiring high radiation resistance. They would indeed provide a high and stable density of interfaces, and thus point defect sinks. These self-organized structures could promote very effectively point defect trapping and recombination, and elimination. As a consequence, such nanostructures would, by design have near perfect radiation resistance.

In the case of highly immiscible alloy systems, e.g., Cu-Nb, Cu-Mo, Cu-W, the above approach needs to be modified since the ballistic mixing is negligible. In this instance, it is impossible to force such alloying elements into solution, in contrast to the moderately immiscible alloy systems such as Cu-Co, Cu- Ag, or Cu-Fe. Recent results reported by Vo et al. [11] indicates that in Cu-base binary Cu-X alloy systems, with X= Nb, Mo, or W, irradiation does in fact induce a nanoscale decomposition. Molecular dynamics simulations suggest that this decomposition takes place during the thermal spike phase of the displacement cascades [11]. The scale of this decomposition is thus limited by the cascade size, typically 1 to 10 nm. This decomposition leads to the formation of highly stable nanostructures, owing to the pinning effects of the precipitates on grain boundaries. It has for instance been reported that Cu-W nanostructures can be stable up to 850 °C, a temperature exceeding 85% of the melting point of Cu.

The new nanostructuring reaction affords novel ways to design materials that are resistant to extreme temperature and irradiation environments. The experimental systems studied so far were all binary alloys, with an elemental precipitating phase (Nb, Mo, or W). In this work, we explore the possibility to extend these results to the more complex case where the precipitating phase is a compound. The model system Cu-(TiB_2) is chosen because of the refractory nature of TiB_2. In addition, Cu-TiB_2 composites may have advantageous mechanical properties, although these will not be investigated in the present work.

CHAPTER 2

BACKGROUND

2.1 Ion Solid Interactions

When high energy particles in the electron volt to mega-electron volt energy range, are bombarding a solid target, they predominantly lose energy through a sequence of elastic two body nuclear collisions with the target atoms and excitation of the electronic system. These elastic collisions are the primary source of damage creation in metals and most semiconductors. The electronic excitations have limited effect on damage production unless the ion energies are in the order of hundreds of mega-electron volt or giga-electron volt range. Electrons mainly act as viscous medium for the motion of the atoms and thus play a critical role as a source of energy dissipation.

2.1.1 Point defects creation

Ion-solid interactions are the cornerstone that guides the broad application of ion beams to the modification of materials. Particle irradiation continues to be a powerful means for investigating the fundamental aspects of defects in solids. Irradiation in materials by energetic particles leads to displacement of atoms from their lattice position to interstitial position generating a vacancy behind, and forming a Frenkel Defect.

When a target atom is struck by a fast moving irradiation particle, atomic displacements begin with the creation of a primary knock on atom (PKA). The energy required to permanently displace a lattice atom presents a threshold, called the displacement energy, E_d. If in the collision process, the energy transferred to the PKA, referred to as the recoil energy, T is far in excess of the displacement energy, E_d the PKA can in turn displace other atoms, secondary knock-on atoms, tertiary knock-ons, etc. –

thus creating a cascade of atomic collisions. If, however $T < E_d$, the impinged atom undergoes large amplitude vibrations without leaving its lattice position and the vibrational energy is shared with the nearest neighbors and dissipates as localized heat. Molecular dynamic simulations reveal that in about 0.2 ps of the creation of PKA, in the highly disturbed localized lattice region, atoms lose their energy and fall below the threshold energy for further displacements, which represents the end of ballistic phase of the cascade. This phenomenon is well illustrated in Fig. 1 as imagined by Seeger in 1958 [12]. At the end of the event, the remnants of the cascade primarily composed of large supersaturations of Frenkel pairs, dislocation loops, redistribution of stresses and extensive mixing of atoms. This is termed as the *primary state of damage*.

The multiple displacement sequence of collision events is referred to as collision or displacement cascade and the average number of atoms displaced in a cascade is known as displacement damage function, denoted by $\langle N_d(E) \rangle$, where E is the energy of the PKA. A schematic of the formation of collision cascade by a PKA is shown in Fig. 2 [13]. The simplest calculation of the damage function, $N_d(E)$ is based on the hard-sphere model of Kinchin and Pease [14]

$$\langle N_d(E) \rangle = \begin{cases} 0 & (if\ E < E_d) \\ 1 & (if\ E_d < E < 2\,E_d \\ \dfrac{E}{2E_d} & (if\ 2\,E_d < E < E_C) \\ \dfrac{E}{2E_d} & (if\ E > E_c) \end{cases}$$

where E_c is a cutoff energy imposed by Kinchin and Pease to accommodate electron energy losses for PKAs at higher energies.

To account correctly for electronic stopping and using a realistic interatomic potential to describe the atomic interactions, Norgett, Robinson and Torrens [15] modified the Kinchin-Pease damage function to

$$\langle N_d \rangle = \frac{\xi\, \nu(E)}{2E_d}$$

where $\xi < 1$ and depends on atomic interactions and $\nu(E)$ is the amount of PKA energy not lost to electronic excitations, commonly referred to as the damage energy. The total modified Kinchin-Pease displacement damage function is given by

$$\langle N_d(E) \rangle = \begin{cases} 0 & (for\ 0 < E < E_d) \\ 1 & (for\ E_d \le E < 2E_d/\xi) \\ \dfrac{\xi\, \nu(E)}{2E_d} & (for\ 2E_d/\xi \le E < \infty) \end{cases}$$

The production and sustenance of a stable Frenkel pair require that the interstitial atom and vacancy are separated by a suitable distance else they would spontaneously recombine. Gibson et al. [16] have shown a region of instability surrounding a vacancy, referred to as spontaneous recombination volume (SRV) which is shown in Fig. 3. SRV determines the energy required for a displacement along with the maximum concentration of defects that can be stored in a lattice. Replacement collision sequence (RCS) is created when an atom replaces the next atom along a close packed row and thus provides a way for transporting interstitial atom beyond the SRV. This is illustrated in Fig. 4 considering a (100) plane of an FCC crystal.

2.1.2 Ion Beam Mixing

In addition to creating point defects, irradiation brings about significant atomic rearrangement. An energetic impinging ion initiates a collision cascade and atoms in the

cascade are mobile enough to undergo rearrangement resulting in an intermixed region [17]. Ion dose, ballistics or kinematics of the ion-target interaction and formation of collision cascade are responsible for ion mixing effect. External factors such as sample temperature during irradiation influence ion mixing.

Guinan and Kinney [18] who studied the displacement events in Tungsten, have divided the temporal development of an energetic cascade into three phases:

(i) A collision phase, refers to when the PKA initiates a collision cascade energy dissipates from each generation of recoils, increasing the cross section for collision. This leads to isotropic mixing of atoms within the cascade and lasts for about a tenth of picosecond.

(ii) A relaxation phase, during which spontaneous recombination of the produced defects takes place, lasting the order of half a picosecond resulting in equilibrium configuration of isolated defects.

(iii) A cooling or "thermal-spike" phase, lasting a few picoseconds during which a highly disordered cascade region eventually achieves local thermal equilibrium with its surroundings.

The three phases can be seen in Fig. 5 where the Frenkel defect concentration is plotted as a function of time in a displacement energy cascade in W, for two different energies (0.6 and 2.5 keV).

"Spike" is defined as a high density cascade which possesses a limited volume in which the majority of atoms are temporarily in motion [19, 20]. Brinkman [21] investigated the damage distribution in a cascade and suggested that a highly disturbed region is formed where every atom is forcefully displaced from its lattice site or PKA

path, producing a volume of material composed of a core of vacancies enveloped by interstitial atoms which is illustrated in Fig. 6.

During thermal spike, depending on the energy density, local temperature can reach or exceed the melting temperature of the material for few picoseconds, giving rise to liquid like diffusion and defect clustering on subsequent cooling [2]. Molecular dynamics simulation of a 10-keV collision event in ordered B_2 phase of NiAl is shown in Fig. 7 [22]. On careful observation a solid-liquid phase boundary can be seen as well.

2.1.3 Radiation Enhanced Diffusion

Following the thermal spike phase, the target system is left with large supersaturation of point defects and defect clusters. Due to the excess point defect concentration atomic mobility is enhanced, as diffusion of an atom is proportional to the probability of having a defect available for its motion [23]. Diffusion coefficient for vacancies is given by,

$$D_V = \Gamma_v d^2/6$$

where Γ_v is vacancy jump frequency, d is atomic jump distance. The atomic diffusion coefficient can now be expressed as,

$$D = f_V C_V D_V$$

where f_V is a correlation factor, C_V is the vacancy concentration. Diffusion under irradiation takes place by the motion of vacancies, interstitials, divacancies etc. In general,

$$D = f_V C_V D_V + f_i C_i D_i + f_{2V} C_{2V} D_{2V} + \ldots.$$

At elevated temperatures, thermal equilibrium vacancy concentration is far in excess of the irradiation-induced defect concentrations and thus thermal diffusion

predominates, nullifying the radiation effects. At intermediate temperatures *D* is nearly independent of temperature and increases linearly with the displacement rate, in what is referred to as sink-limited regime as most of the point defects are lost at defect sinks. At even lower temperatures, irradiation induced vacancy concentration is high enough that, direct recombination with interstitials dominates over diffusion to fixed sinks. This can be summarized in a schematic plot shown in Fig. 8. [24].

2.2 Driven Alloys

Materials that are continuously maintained away from thermodynamic equilibrium by external driving force are generally referred to as driven systems. Materials under irradiation, or subjected to constant plastic deformation under cyclic fatigue or ball milling, are examples of driven systems [25]. Neglecting the medium and long-range relocations due to nuclear collisions, Martin's effective temperature model [6] explains the phase behavior of driven systems. In this model, $T_{eff} = T\ (1+ \Delta)$, where Δ is ratio of atomic jumps from the ballistic events to atomic jumps from thermally activated events. In an immiscible alloy under irradiation, there exists a dynamic competition between the two diffusion processes and thus Δ is a relative measure of their strengths. At high irradiation flux and low temperatures, Δ is large and the system behaves as if it was effectively at a high temperature. This effective temperature model relates dynamical steady states to effective equilibrium states, making possible to construct a map of stable steady states as a function of irradiation parameters.

The microstructure of driven systems may spontaneously self-organize during sustained forcing [26]. Pattern formation in irradiated alloys concerns spatial organization

of defects such as void clusters, dislocations along with compositional spatial organization and chemical order [26, 27].

Extending the results of the effective temperature model, Enrique and Bellon, predicted that in moderately immiscible systems irradiated at intermediate temperatures or ballistic relocation rates, a steady state self organization at mesoscopic scale, known as compositional patterning can be observed [8, 28]. The model takes into account the effects of two control parameters, the average relocation distance, R and the reduced ballistic mixing, γ. The corresponding dynamic phase diagram is shown in Fig. 9.

However, in case of highly immiscible alloy systems, another case of nanostructuring has been recently identified which is almost independent of temperature and where nanoprecipitation takes place within the displacement cascades [11]. Based on the experimental results and molecular simulations, Vo et al. proposed that the migration of solute atoms in the liquid phase of the thermal spike results in the precipitation of the nanoscale particles whose maximum size is comparable to size of the melt zones ~ 5 nm in Cu-Mo or in Cu-W.

2.3 Dilute immiscible Cu alloys

Due to their high thermal conductivity, Cu-base alloys find applications as first wall materials in future reactors. Due to their thermal stability Cu alloys are potential interconnect materials in semiconductor industry. From a fundamental perspective, Cu-base alloys are excellent model materials, owing to the wide range of accessible heat of mixing, ranging from nearly ideal solid solutions, e.g., Cu-Ni, to moderately immiscible systems, e.g. Cu-Ag, Cu-Co, Cu-Fe, to highly immiscible systems such as Cu-Nb, Cu-Mo, and Cu-W. In the latter case, elements are in fact immiscible in the solid state as well

as in the liquid state. This wide variety of immiscibility can be used to probe to the intensity and characteristics of the mixing forced by irradiation, and to achieve nanostructuring. This work focuses on the Cu-TiB_2, and aims at exploring the possibility of inducing by ion irradiation a stable dispersion of TiB_2 nanoprecipitates in Cu.

(i) Cu-Ag: Ag has a solubility of less than 0.1% at room temperature and about 8.8% at eutectic temperature. For irradiation temperatures below ~120 °C, no Ag precipitation was observed, however thermal precipitation was significant above ~200 °C. Cu-Ag alloy showed a maximum temperature for the self-organization around 175 °C to 200 °C. Also observed was the dissolution of the phase separated microstructure, under low temperature irradiation [5]. Enrique et al. have showed through experiments and simulations, that Cu-Ag composites undergo compositional patterning under specified conditions of temperature and irradiation does [7, 8]. Other results on irradiation of Cu-Ag alloy at 250 °C showed solute enrichment on either side of the grain boundaries, but depletion at the grain boundary due to the solute segregation, which is expected for oversized Ag atoms [24].

(ii) Cu-Co: This system parallels the Cu-Ag, but the maximum solubility of Co in Cu is less, making this system more immiscible, and the boundary separating pattering and coarsening regime is about ~150 °C higher than the $Cu_{85}Ag_{15}$. Magnetization measurements reported by Krasnochchekov et al. [9] yield the size of precipitates as a function of irradiation temperatures. The three possible steady states expected from the dynamical phase diagram Fig. 9 were observed experimentally. It was also observed that the patterning regime is independent of

initial conditions. The variation of particle size with irradiation dose for $Cu_{85}Co_{15}$ is shown in Fig. 10.

(iii) Cu-Fe: This system is comparable to Cu-Co ,as the Fe solubility is less than 0.1 at% at room temperature and increases to ~4 at% at peritectic temperature (1085°C), and at early stages of the precipitation, Fe forms coherent fcc precipitates in Cu. An APT study revealed that nanostructured steady states existed between room temperature and 300 °C. As in Cu-Ag, Cu-Co, the precipitate size during irradiation in patterning regime was independent of initial conditions [10]. Atom Probe Tomography results are shown in Fig. 11.

(iv) Cu-Nb: Cu and Nb have negligible mutual solubility in the solid state, and liquid Cu in immiscible with solid Nb, but Cu and Nb liquids are largely miscible. Averback et al. showed with the help of RBS that small mixing was detected at 6 K however, none at 295 K emphasizing the effects of mixing due to ballistic cascades [29]. It is believed that during the phase of thermal spike, a liquid like melt created would facilitate the movement of the Nb atoms leading to the formation of nanostructures. Experimental evidence from Chee et al. [10] show that the precipitate size remained constant at high temperature and irradiation conditions, unlike the above mentioned systems.

(v) Cu-Mo: Mo is also highly immiscible in Cu, both in the solid and in the liquid state. It was shown that there was no mixing even at temperatures below liquid nitrogen (6 K) and room temperature (295 K) [29]. Vo et al. [11] have reported Mo begins to precipitate thermally at about ~400 °C and remains stable until about $0.65T_m$ (T_m is the melting temperature of Cu, ~1083 °C) after which

significant coarsening is observed. Under irradiation, Mo precipitates at room temperature but does not coarsen until high temperatures. Such a thermal stability can be explained by low atomic diffusivity combined with small solubility and Zener pinning at grain boundaries [30].

(vi) Cu-W: Cu-W system is similar to Cu-Mo W being highly immiscible and having low tracer diffusivity. $Cu_{90}W_{10}$ films do not undergo precipitation until about ~550 °C and then remains stable until 0.85 T_m, after which significant coarsening is observed. This is illustrated in Fig.12. As in Cu-Mo, irradiation at room temperature and above leads to nanoscale precipitation of the W phase. These results can be understood as during irradiation, at temperatures low enough for thermal diffusion to be neglected, particle size and grain size is controlled by the size of the thermal spike region, and at higher temperatures, thermal coarsening becomes dominant.

2.4 TiB_2 and the Cu-TiB_2 alloy system

Titanium diboride (TiB_2) is one of the most stable titanium-boron compounds and an extremely hard (~25-35 GPa at room temperature) ceramic compound having a high melting temperature, 3225 °C. TiB_2 crystallizes as hexagonal close packed, P6/mmm space group with lattice parameters of a = 302.36 pm and c = 322.04 pm and has low density (4.52g/cc). In contrast to many ceramics it has high thermal conductivity (60-120 W/mK) and a high electrical conductivity (~10^5 S/cm). Due to these properties mentioned above, it has several applications ranging from impact resistant armor, cutting tools and wear resistant coatings [31].

A binary phase diagram of Ti-B is shown in Fig. 13 calculated with Thermo-calc software [32]. There is no information available in literature about the Cu-Ti-B ternary phase diagram or the thermodynamic data. It is however instructive to analyze the calculated Ni-Ti-B and Fe-Ti-B phase diagram [33]. The Ni-Ti-B phase diagram, Fig. 14 shows that, in the Ni-rich corner, phase coexistence can take place between the Ni-rich fcc solid solution and several compound phases, including Ni_3B, Ni_3Ti and the so-called τ (fcc) $Ti_3Ni_{20}B_6$ phase. The formation of the TiB_2 phase at 800 °C requires a rather large concentration of Ti (>25%) and B (>25%). It should be noticed, however, that Ni and B have a negative heat of mixing and form multiple compounds, where as Cu and B are immiscible. Fe and B do also form compounds, but the ternary Fe-Ti-B phase diagram, see also the Fe-TiB_2 pseudo binary phase diagram in Fig. 15, indicates that an iron solid solution can coexist with TiB_2 below ≈1300 °C, as well as Fe_2B for low Ti content. In this present work, we investigate first whether TiB_2, when added to a Cu base, can form stable nanoprecipitates, under irradiation. If such precipitation takes place, as we will show, the second question that we address is whether this nanostructuring is similar to the one taking place in the Cu-Ag, Cu-Co or Cu-Fe systems discussed above, or to that identified in the Cu-Nb, Cu-Mo or Cu-W alloy systems. In order to investigate the behavior, we have grown thin films, co-sputtered and multilayered. We have characterized them primarily by transmission electron microscopy, with additional characterization done by XRD and RBS, before and after irradiation using 1.8 MeV Kr ions, with doses ranging from 1×10^{16} ions/ cm^{-2} to 3×10^{16} ions/ cm^{-2} and irradiation temperatures from the room temperature to 800 °C.

CHAPTER 3

EXPERIMENTAL METHODS

3.1 Sample Preparation and Irradiation

Pure Cu, pure TiB_2, Cu-TiB_2 multilayers, and Cu-TiB_2 co-sputtered thin film specimens were grown on oxidized Si wafers in AJA ATC 1200 DC magnetron sputtering system equipped with a Cu target (Kurt. J. Lesker, 99.999% purity, 1.5" diameter and 0.125" thick) and a TiB_2 target (Optical Coating Material, 99.5% purity, 1.5" diameter and 0.125" thick). The base pressure in the growth chamber was $\approx 4 \times 10^{-8}$ Torr, and the operating pressure during growth was $\approx 2 \times 10^{-3}$ Torr Ar. The growth chamber is equipped with a load lock chamber and the samples are loaded on the Inconel sample stage and transferred using a magnetic rod from the load lock chamber into the growth chamber once the load lock pressure falls below 1×10^{-6} Torr. The specimen stage was positioned at ≈ 10 cm from the magnetron sources to have minimum thickness and concentration variation. The film thicknesses were ≈ 200 nm, which is less than the projected range of Kr ions, ≈ 300 nm as calculated using TRIM [34]. The multilayered samples consisted of alternation layers of Cu (thickness of 16 nm) and TiB_2 (thickness of 4 nm), with 10 periods. The co-sputtered thin films were grown to match the composition of $Cu_{0.85}(TiB_2)_{0.15}$ and some of the co-sputtered samples were capped with a 10 nm layer of TiB_2 to suppress oxidation during irradiation at large doses. A schematic cartoon of the two sample types is shown in Fig. 16.

Irradiations were carried out using 1.8 MeV Kr ions in HVE Van de Graaff accelerator at the Frederick Seitz Materials Research Laboratory. Irradiation chamber was maintained $\approx 5 \times 10^{-8}$ Torr during heating and irradiation, and a high vacuum was

maintained by filling the cold finger with liquid nitrogen at regular intervals during the run. The ion beam was rastered using x-y deflector plates and passed through a 3 mm aperture before entering the target chamber. The beam current was maintained at ~ 100 nA, which restricted beam heating to less than ~ 10 °C. The deposited damage energy is nearly uniform throughout the entire film, increasing by ~ 30% from the front to back sides of the film. The results reported here were obtained after irradiation doses of 1×10^{16} ions/ cm^{-2} and 3×10^{16} ions/ cm^{-2} which corresponds to 25 and 75 displacements per atom (dpa), as determined by SRIM calculations [34].

3.2Characterization of Microstructure

The following analyzing techniques were used to characterize the alloy thin films in this work.

3.2.1 X-Ray Diffraction (XRD)

The X-ray diffraction measurements were performed using a Philips X'pert MRD system using a Cu X-ray source with point focus optics operated at 45 kV and 40 mA. The X-rays travel through the Ni filter to remove K_β signal and 1 mm × 3 mm exit slit before hitting the sample. The samples were aligned using the Si (0 0 4) peak and omega-2theta scans were performed with a step size of 0.02° step size and a scan speed of 2-10 seconds per step.

3.2.2 Rutherford Backscattering (RBS)

Rutherford backscattering (RBS) measurements were performed with the HVE Van de Graaff accelerator with a beam of 2 MeV He^+ ions passed through a circular aperture before hitting the sample. The thickness and composition of the thin film samples was estimated using the RBS measurements and analyzed using the RBS fitting

software SIMNRA [35]. The incident beam was aligned at an angle of 22.5° to the sample normal and the solid state detector is positioned 30° relative to the incident beam and thus the scattering angles was 150°.

3.2.3 Transmission Electron Microscopy (TEM) and Scanning Transmission Electron Microscopy (STEM)

Transmission electron microscopy was performed using a JEOL 2100 Cryo with LaB_6 filament for bright field (BF) and dark field (DF) imaging, and electron diffraction. For high-angle annular dark field (HAADF), high resolution (HREM) and energy dispersive spectroscopy (EDS) measurements, JEOL 2010F with a field emission gun operating at200kV was used.

The cross sectional samples were prepared both by conventional method and by focused ion beam (FIB) using a Ga beam in FEI Dual Beam 235 FIB. In the conventional technique, two thin strips of the samples ~1.5 mm wide are cut using a low speed diamond saw and then cleaned using an ultrasonic cleaner. The two thin strips were glued films facing each other using M-Bond epoxy and cured under constant pressure at 120°C. The sample was then mounted on a tripod stand, ground and polished on both sides using boron carbide powder and diamond lapping films to a thickness of ≈ 50 microns and then mounted on to a TEM grid. The cross section sample was then ion milled to electron transparency using a GATAN Precision Ion Polishing System (PIPS) at room temperature. Samples prepared using the FIB lift-out technique followed the process described by Langford et al. [36] showing the different steps in Fig. 17. The thin cross section was lifted and welded on a TEM grid using the Pt source. However, no major differences were observed in the cross sections prepared by both the techniques.

CHAPTER 4

RESULTS

4. 1 Irradiation of pure TiB_2 thin films

It is known from prior work [37], that TiB_2 grown by magnetron sputtering of a TiB_2 target on a Si substrate, at room temperature and in absence of external bias would result in an amorphous structure. Upon irradiation with 1.8 MeV Kr^+ ions at high temperature, 800 °C, electron diffraction demonstrated that the amorphous phase transformed to the equilibrium hexagonal TiB_2 phase as seen in Fig. 18. We note that this phase was not detected by XRD, probably because of low atomic numbers of Ti and B. Dark field imaging of the irradiated TiB_2 sample indicated that the grains of the order 20 to 30 nm as illustrated in Fig. 19. A bright field image and a high resolution electron micrograph of the irradiated sample at 3×10^{16} ions/ cm^{-2} are shown in Fig. 20 and Fig. 21.

4.2. Irradiation of Cu/ TiB_2 multilayers

Alternate layers of Cu and TiB_2 each measuring 16 nm and 4 nm respectively were grown on Si/SiO_2 substrate until a thickness of ~ 200 nm was deposited. It was observed that the Cu layers were crystalline with grains growing up to the thickness of the layer (~ 16 nm) and TiB_2 layers were amorphous as expected as seen in Fig. 22. Twinning was commonly observed in Cu layers and the interfaces remained fairly abrupt with a small amount of roughness, of the order 2 to 3 nm as seen in Fig. 23. The electron diffraction pattern in Fig. 24 shows the presence of only Cu reflections but no TiB_2 reflections. After irradiation at 650 °C with an ion dose of 3×10^{16} ions/ cm^{-2} as illustrated by Fig. 25, the main change was the crystallization of the TiB_2 layer, forming

the equilibrium hexagonal TiB_2 phase. A highly magnified image, Fig. 26, of the irradiated multilayer sample showed that the interface was highly stable and had no significant increase of mixing or roughness was observed. This confirms the result from Basu et al. [38] who showed the remarkable interface stability of Cu/ TiB_2 under 400 keV Ne^{++} irradiation at room temperature. It was interesting to note that we did not observe any radiation damage observed despite high irradiation dose.

4.3 Irradiation of co-sputtered $Cu_{0.85}(TiB_2)_{0.15}$ thin films

A dilute Cu alloy with about ~ 15% second phase particle was considered as, if precipitation of TiB_2 would take place, it would most likely result in isolated particles dispersed in the matrix, thus facilitating their characterization. A single layer of homogeneous solid solution of Ti and B in Cu matrix was grown at room temperature. As seen in the electron diffraction pattern Fig. 27, only FCC Cu reflections were observed with no signs of TiB_2 reflections. A high angle annular dark field (HAADF) image of the as grown sample is shown in Fig. 28 and as expected a uniform gray contrast is seen.

In contrast, HAADF imaging, see Fig. 29 of the sample irradiated at a fluence of 3×10^{16} ions/ cm^{-2} at room temperature (~25 °C) showed the presence of a second phase precipitate with a darker contrast, thus lighter than the matrix. When the irradiation temperature was increased to 650 °C and irradiated with a dose of 1×10^{16} ions/ cm^{-2} Kr^{+} ions, the spherical zones with darker contrast were also observed uniformly throughout the sample in HAADF images, as seen in Fig. 30. A second phase was identified from electron diffraction as shown in Fig. 31. All the extra diffraction peaks matched the peaks of TiB_2, in particular the $\{10\bar{1}0\}$ and $\{10\bar{1}1\}$ reflections. It was verified that the reflections did not match any other possible phases such as TiB, TiO_2 etc. The electron

diffraction results are thus strong indication that the phase precipitated at elevated temperature was TiB_2. The spherical zones were uniformly distributed throughout the thickness of the film. The zones appeared darker than the background, thus corresponding to regions with average atomic number lower than that of Cu matrix. We thus conclude that these spherical zones, 4 to 5 nm in diameter, are TiB_2 precipitates.

Irradiation at a dose 3 times larger, 3×10^{16} ions/ cm^{-2}, were carried out to determine if the above microstructure had reached a steady state. When using standard co-sputtered samples, some unexpected changes were observed, in particular a decrease of the size of the dark zones in HAADF images, and a change in the position of the extra reflections in the diffraction patterns. It was suspected that oxidation in the irradiation chamber could have contributed to these unexpected features, so a new set of samples was grown by capping the $Cu_{0.85}(TiB_2)_{0.15}$ film with a 10 nm TiB_2 layer to suppress oxidation during irradiation. Irradiation of the Cu/TiB_2 multilayers, see section 4.2, suggested that such a capping layer would be stable and effective. Irradiation of these capped co-sputtered samples to 3×10^{16} ions/ cm^{-2} produced a microstructure that could not be distinguished from the one observed after 1×10^{16} ions/ cm^{-2}. In particular the size of the dark zones in HAADF was unchanged, at ≈ 5 nm, as seen in Fig. 32. The extra reflections detected in the electron diffraction pattern were also indexed as $\{10\bar{1}0\}$ and $\{10\bar{1}1\}$ TiB_2 as shown in Fig. 33.

CHAPTER 5

DISCUSSION

Careful analysis of the microscopy results, of the as-grown and irradiated samples at different temperatures and irradiation doses, lead to the conclusion that irradiation can trigger nanostructuring in the Cu-TiB_2 alloy system. Nanoprecipitation of TiB_2 phase is evidenced by electron diffraction even at irradiation temperatures as low as room temperatures, where thermal diffusion of Ti and B is negligible, indicating that the decomposition takes place in displacement cascades, probably during the thermal spike phase. The number density of the dark zones in the HAADF image was estimated by counting them over large areas (typically 50 nm by 50 nm), and with the help of electron energy loss spectroscopy (EELS) to determine foil thickness, ≈ 42 nm for the area shown in Fig. 28. The number density was estimated to be $\approx 3.3 \times 10^{23}$ m^{-3} for irradiation to 3×10^{16} ions/ cm^{-2}, which corresponds to a volume fraction of 2.2% if we assume a constant diameter of 5 nm for all spherical zones. A nearly identical particle density, $\approx 1.9 \times 10^{23}$ m^{-3} was found for irradiation dose of 3×10^{16} ions/ cm^{-2}. We thus conclude that the nanostructuring induced by the precipitation of TiB_2 had reached steady state (or at least a quasi steady state).

The results presented in Chapter 4 establish that the irradiation of the co-sputtered Cu-TiB_2 thin films led to the formation of TiB_2 nanoprecipitates, with an average size of $\approx$ 5 nm and a number density $\approx 3.3 \times 10^{23}$ m^{-3}. Starting from fairly homogeneous $Cu_{.85}(TiB_2)_{.15}$ solid solutions (see Fig. 28) this nanoscale precipitation was observed after irradiation at room temperature (Fig. 29) and at 650 °C (Fig. 28), with no significant difference in precipitate size or number density. In addition, for irradiations at 650 °C, the

size and number density did not evolve significantly with a three fold increase of the irradiation dose, from 1×10^{16} ions/ cm^{-2} to 3×10^{16} ions/ cm^{-2} (75 dpa), indicating that the nanoscale precipitation had reached a steady state under irradiation (Fig. 32). The identification of the precipitating phase relied on its darker contrast in HAADF (thus corresponding to a lower average atomic number than the matrix), on the larger Ti concentration in these dark regions when analyzed by EDS, and on the presence of TiB_2 diffraction spots in electron diffraction patterns. Attempts were made to image directly the TiB_2 precipitates by the dark field imaging but no conclusive results could be obtained due to the weak intensity of the TiB_2 reflections and their overlap with the Cu reflections. It is nevertheless believed that the results reported here convincingly establish the nature of the precipitates as hexagonal TiB_2.

The irradiation-induced precipitation in Cu-TiB_2 identified in this work displays the three key characteristics of nanostructuring induced by displacement cascades as reported earlier for highly immiscible systems such as Cu-Nb, Cu-Mo and Cu-W [11]. First, (i) the TiB_2 precipitate size is about the size of the largest displacement cascades in Cu (≈ 5 nm), and it is essentially independent of irradiation temperature (here 25 °C to 650 °C), at temperatures low enough for thermal precipitate coarsening to be negligible. Second, (ii) ballistic mixing does not play a significant role, as illustrated by the fact that RT irradiation does in fact induce the formation of precipitates in an initially homogeneous alloy. The lack of significant ballistic mixing is consistent with the results reported by Basu et al. [38] after irradiation of Cu/ TiB_2 multilayers with 400 keV Ne ions at room temperature to a maximum dose of 1.2×10^{16} ions/ cm^{-2} (≈ 5 dpa). Third, (iii) the nanostructuring has reached a steady state, as both the precipitate size and their

number density did not change significantly when the irradiation was increased threefold, from 1×10^{16} ions/ cm^{-2} to 3×10^{16} ions/ cm^{-2}. It is also worth noting that the points (i) and (ii) clearly establish that this nanostructuring cannot result from a dynamical competition between dissolution promoted by ballistic mixing and precipitation driven by thermally activated decomposition.

The volume fraction of precipitated TiB_2 was estimated to be $\approx 2\%$, based on an average precipitate size of 5 nm and an average number density of 3×10^{23} m^{-3}. This volume fraction is lower than the as-grown volume fraction of TiB_2, 15%. This indicates that not all Ti and B atoms are participating to the formation of nanoprecipitates, in contrast to the case of binary immiscible alloy systems such as Cu-Mo or Cu-W. This is interesting since the largest irradiation dose employed here leads to many overlapping cascades. A possible kinetic limitation in the formation of TiB_2 during thermal spikes comes from its somewhat complex hexagonal crystallographic structure, with alternating layers of Ti and B. It should be noted that an important difference between the present system and highly immiscible binary systems such as Cu-W is that additional atomic interactions are involved because we are dealing with a ternary alloy system. In particular, Cu and Ti possess a negative heat of mixing, -19 kJ/ g.atom for the equiatomic composition, and it is thus conceivable that some Ti remains in solution during the thermal spike phase of displacement cascades, despite the much higher negative heat of formation of TiB_2, -94 kJ/ g.atom [33]. The presence of Ti in solution is supported by the EDS analysis of the matrix, which yielded a significant amount of Ti, about 3-4 % (B cannot be quantified with the EDS system used in this study). No Cu-Ti compounds or

amorphous phase were observed before or after irradiation, although the formation of a small amount of such phases cannot be excluded.

In addition to the nanostructuring observed in the co-sputtered samples after irradiation, it is interesting to note that large extended defects such as dislocation loops were not observed in Cu matrix. An interesting result from the XRD was the small grain size in irradiated samples over a large range of temperatures, Fig. 34. A grain size of about ≈ 30 nm was maintained even at ~ 0.7 T_m of Cu indicating good microstructural stability. A comparison of the XRD patterns of the co-sputtered and multilayered samples in shown in Fig. 35. These results suggest that either the TiB_2 nanoprecipitates or the Ti and B in the solution are effective in suppressing grain growth. It is concluded that nanoprecipitation of TiB_2 imparted high radiation resistance to Cu.

Several research directions could be pursued to expand on the present results. Firstly, it would be interesting to investigate whether the nanostructured Cu-TiB_2 microstructure provides effective resistance against swelling, that is whether it can trap He atoms in small bubbles. This could be studied by implanting large doses of He and determining the local concentration of He required for bubbles to form, as well as their size, location in relationship to the nanostructure, and their number density. Similarly studies have been conducted for Cu/Nb and Cu/ V multilayers [39] and for nano-ODS steels [40]. One would hope that He would be confined in small bubbles at the Cu/TiB_2 interfaces, thus suppressing swelling.

Another direction of future research would be to investigate another ternary alloy system. Interestingly enough, preliminary results conducted in our research group on Ni-TiB_2 seem to indicate that irradiation does not induce nanoprecipitation of TiB_2 in a Ni

matrix. As indicated in Chapter 3, the equilibrium phase diagram of the Ni-Ti-B system, in the Ni-rich corner, suggests however that several phases may form before TiB_2, including Ni_3Ti, Ni_3B, and the τ phase. This complexity, which is apparently absent in Cu-Ti-B, possibly because of the positive heat of mixing in Cu-B in contrast to the negative heat of mixing of Ni-B, may explain why the TiB_2 phase does not form during irradiation of Ni-TiB_2 thin films. The Fe-Ti-B system would also be of interest, as the Fe-rich corner of the equilibrium phase diagram of the system suggests that co-existence between Fe and TiB_2 can be achieved at low TiB_2/ Fe ratios. Lastly, another extension of the present work would be to investigate the model systems comprised of metallic matrix containing oxide phases, owing to the large interest in radiation resistance of nano-ODS steels. This extension will however require a different growth technique owing to the poor electric conductivity of oxides.

CHAPTER 6

CONCLUSIONS

In this thesis, we have studied the evolution of the microstructure of Cu-TiB_2 thin films after large dose of irradiation with 1.8 MeV Kr ions, for irradiation temperatures ranging from room temperature to 800 °C. The main result of this work is that irradiation can induce nanoprecipitation of TiB_2 in the Cu matrix. The TiB_2 precipitates, identified by the electron diffraction and EDS analysis, were imaged by HAADF-TEM. Their average diameter was determined to be ≈ 5 nm, and their number density $2\text{-}3 \times 10^{23}$ m^{-3}. By comparing thin films irradiated to 1×10^{16} ions/ cm^{-2}(≈ 25 dpa) and 3×10^{16} ions/ cm^{-2} (≈ 75 dpa), it was established that this precipitation reaction led to a steady state nanostructured material. In addition, as nearly identical nanostructures formed during irradiation at room temperature and at 650 °C, it is concluded that this irradiation-induced nanostructuring is similar to one recently reported in highly immiscible binary systems such as Cu-Mo and Cu-W. It is thus proposed that this nanostructuring takes place during the thermal spike phase of displacement cascades, and is thus largely independent if the irradiation temperatures. We observed also that nanostructuring is very effective in suppressing grain growth even at very high temperatures, as also reported in Cu-W. The present results are novel in the sense that they establish that precipitation in displacement cascades can not only lead to the formation of elemental secondary phase, as in Cu-W, but also to the formation of compounds, here TiB_2. These results suggest that it would be interesting to extend the present study by investigating other metal-diboride systems, and possibly in metal-oxide systems as well. Such studies should be helpful in developing the

science needed, for instance, for elucidating the stability of nanoscale oxide precipitates in nano-ODS steels, and for designing alloys with improved radiation resistance.

The results reported in this thesis have been partially presented in a poster at the 2011 Annual TMS conference in San Diego CA, receiving the best poster award. A manuscript is in the final stages of precipitation and will be submitted for publication in Journal of Nuclear Materials.

CHAPTER 7

REFERENCES

1. Robinson, M. T., Basic physics of radiation damage production, *Journal of Nuclear Materials,* Vol. 216, 1994, pp. 1-28
2. Averback, R. S., and T. D. De La Rubia, Displacement damage in irradiated metals and semiconductors, *Solid State Physics,* Vol. 51, 1998, pp. 281-402
3. Dhara, S., Formation, dynamics, and characterization of nanostructures by ion beam irradiation, *Critical Reviews in Solid State & Materials Science,* Vol. 32 (1/2), 2007, pp. 1-50
4. Roberto, J. and T. D. De La Rubia, Basic research needs for advanced nuclear energy systems, *JOM Journal of the Minerals, Metals and Materials Society,* Vol. 59 (4), 2007, pp. 16-19
5. Chee, S. W., Self-organization of dilute Cu binary alloys under ion irradiations, Pd.D. Dissertation, University of Illinois at Urbana-Champaign, 2008
6. Martin, G., Phase stability under irradiation: Ballistic effects, Physical Review B, Vol. 30 (3), 1984, pp.1424- 1436
7. Enrique, R. A., K. Nordlund, R. S. Averback and P. Bellon, Simulations of dynamical stabilization of Ag-Cu nanocomposites by ion beam processing, *Journal of Applied Physics,* Vol. 93, 2003, pp. 2917- 2923
8. Enrique, R. A., and P. Bellon, Compositional patterning in systems driven by competing dynamics of different length scale, *Physical Review Letters,* Vol. 84 (13), 2000, pp. 2885-2888

9. Krasnochchekov, P., R. S. Averback and P. Bellon, Phase separation and dynamic patterning in $Cu_{1-x}Co_x$ films under irradiation, *Physical Review B,* Vol. 72 (17), 2005, pp. 1-12

10. Chee, S. W., B. Stumphy, N. Q. Vo, R. S. Averback and P. Bellon, Dynamic self-organization in Cu alloys under ion irradiation, *Acta Materialia,* Vol. 58, 2010, 4088- 4099

11. Vo, N. Q., S. W. Chee, D. Schwen, X. Zhang, P. Bellon and R. S. Averback, Microstructural stability of nanostructured Cu alloys during high-temperature irradiation, *Scripta Materialia,* Vol. 63, 2010, 929- 932

12. Seeger, A., *Proceedings 2nd UN International Conference on Peaceful Uses of Atomic Energy,* Vol. 6, 1958, pp. 20

13. Thompson, M. W., Defects and radiation damage in metals, Cambridge University Press, 1969

14. Kinchin, G.H., and R. S. Pease, The displacements of atoms in solids by radiation, *Report of Progress in Physics,*Vol. 18, 1955, pp. 1

15. Norgett, M. J., M. T. Robinson, and I. M. Torrens, A proposed method of calculating displacement dose rates, *Nuclear Engineering Design*, Vol. 33, 1975, pp. 50

16. Gibson, J. B., A. N. Goland, M. Milgram, and G. H. Vineyard, Dynamics of radiation damage, *Physical Review,* Vol. 120 (4), pp.1229-1253

17. Nastasi, M., and J. W. Mayer, Ion beam mixing in metallic and semiconductor materials, *Materials Science and Engineering,* Vol. 12, 1994, pp. 1-52

18. Guinan, M. W., and J. H. Kinney, Molecular dynamic calculations of energetic displacement cascades , *Journal of Nuclear Materials,* Vol. 103/104, 1981, pp. 1319- 1323
19. Sietz, F., and J. S. Koehler, Displacement of atoms during irradiation, *Solid State Physics,* Academic Press, Vol. 2, 1956, pp.305
20. Sigmund, P., Energy density and time constant of heavy-ion-induced-elastic-collision spikes in solids, *Applied Physics Letters,* Vol. 25, 1974, pp. 169
21. Brinkman, J. A., Production of atomic displacements by high energy particles, *American Journal of Physics,* Vol. 24, 1956, pp. 246
22. Zhu, H. L., R. S. Averback, and M. Nastasi, Molecular dynamics simulations of a 10-keV cascade in beta-NiAl , *Philosophical Magazine A-Physics of Condensed Matter Structure defects and mechanical properties*, Vol. 71 (4), 1995, pp. 735-738
23. Sizmann, R., Effect of radiation upon diffusion in metals, *Journal of Nuclear Materials,* Vol. 69-70 (1-2), 1978, pp. 386-412
24. Russell, K. C., Phase-stability under irradiation, *Progress in Materials Science*, Vol. 28 (3-4), 1984, pp. 229-434.
25. Martin. G., and P. Bellon, Driven alloys, *Solid State Physics,* Vol. 50, 1997, pp. 189-331
26. Bellon, P., and R. S. Averback, Preface to viewpoint set on : materials under driving forces, *Scripta Materialia,* Vol. 49, 2003, 921-925

27. Ye, J., and P. Bellon, Nanoscale patterning of chemical order induced by displacement cascades in irradiated alloys. I. A. kinetic monte carlo study, *Physical Review B,* Vol. 70 (094104), 2004, pp. 1-11.

28. Enrique, R. A., and P. Bellon, Compositional patterning in immiscible alloys driven by irradiation, *Physical Review B,* Vol. 63 (134111), pp. 1-12

29. Averback, R. S., D. Peak, and L. J. Thompson, Ion-beam mixing in pure and in immiscible copper bilayer systems, *Applied Physics A: Surfaces and Solids,* Vol, 39, 1986, pp. 59-64

30. Nes, E., N. Ryum, and O, Hunderi, On the Zener drag, *Acta Metallurgica,* Vol. 33, 1985, pp. 11-22

31. http://en.wikipedia.org/wiki/Titanium_diboride

32. http://www.calphad.com/titanium-boron.html

33. http://www.springermaterials.com/navigation/index.html, The Landolt-Bornstein Database, *Springer Materials,* 2011

34. Ziegler, J. F., J. P. Biersack, and U. Littmark, The Stopping and Range of ions in Matter, *Pergamon,* 1985.

35. Mayer, M., *SIMNRA,* [SIMNRA, a simulation program for the analysis of NRA, RBS and ERDA]. Available from www.rzg.mpg.de/~mam

36. Langford, R. M., and A. K. Petford-Long, Preparation of transmission electron microscopy cross-section specimens using focused ion beam miling, *Journal of Vacuum Science and Technology A,* Vol. 19 (5), 2001, pp. 2186- 2193

37. Deng, H., J. Chen, R. B. Inturi, and J. A. Barnard, Structural, mechanical and tribological properties of d.c. magnetron sputtered TiB_2 and TiB_2(N) thin films, *Surface and Coatings Technology,* Vol (76/77), 1995, pp. 609 – 614

38. Basu, S. N., M. Hubbard, J. P. Hirvonen, T. E. Mitchell and M. Nastasi, Microstructure and stability of TiB_2 and Cu multilayers, *Materials Research Society Symposium Proceddings,* Vol. 187, 1990, pp. 157- 160

39. Demkowicz, M. J., D. Bhattacharyya, I. Usov, Y. Q. Wang, M. Nastasi, A. Misra, The effect of excess atomic volume on He bubble formation at fcc-bcc interfaces, *Applied Physics Letters,* Vol. 97 (16), 2010, pp. 161903-1-3

40. Hsiung, L., M. Fluss, S. Tumey, J. Kuntz, B. El-Dasher, M. Wall, B. Choi, A. Kimura, F. Willaime, Y. Serruys, HRTEM study of oxide nanoparticles in K3-ODS ferritic stell developed for radiation tolerance, *Journal of Nuclear Materials*, Vol. 409 (2), 2011, pp. 72-79

CHAPTER 8

FIGURES

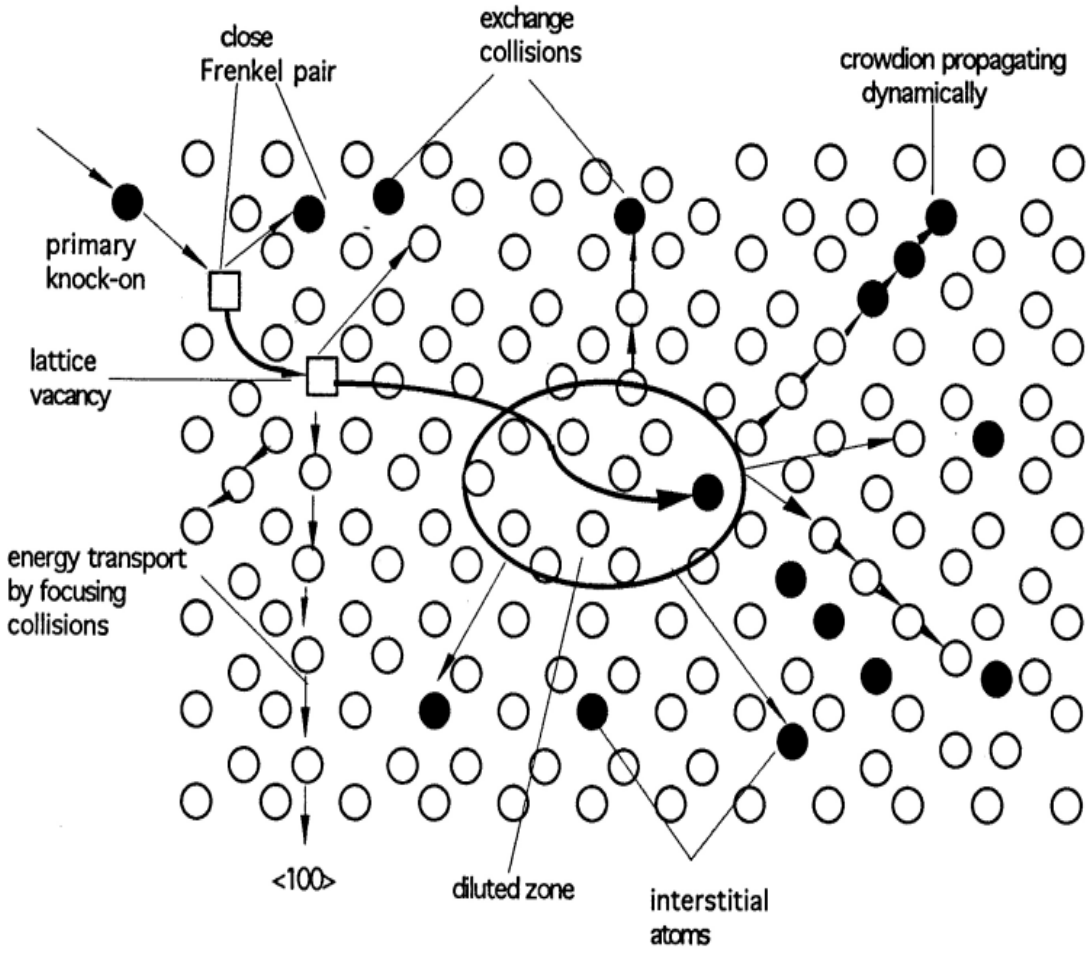

Figure 1. Atomic displacement process in energetic displacement cascade. [12]

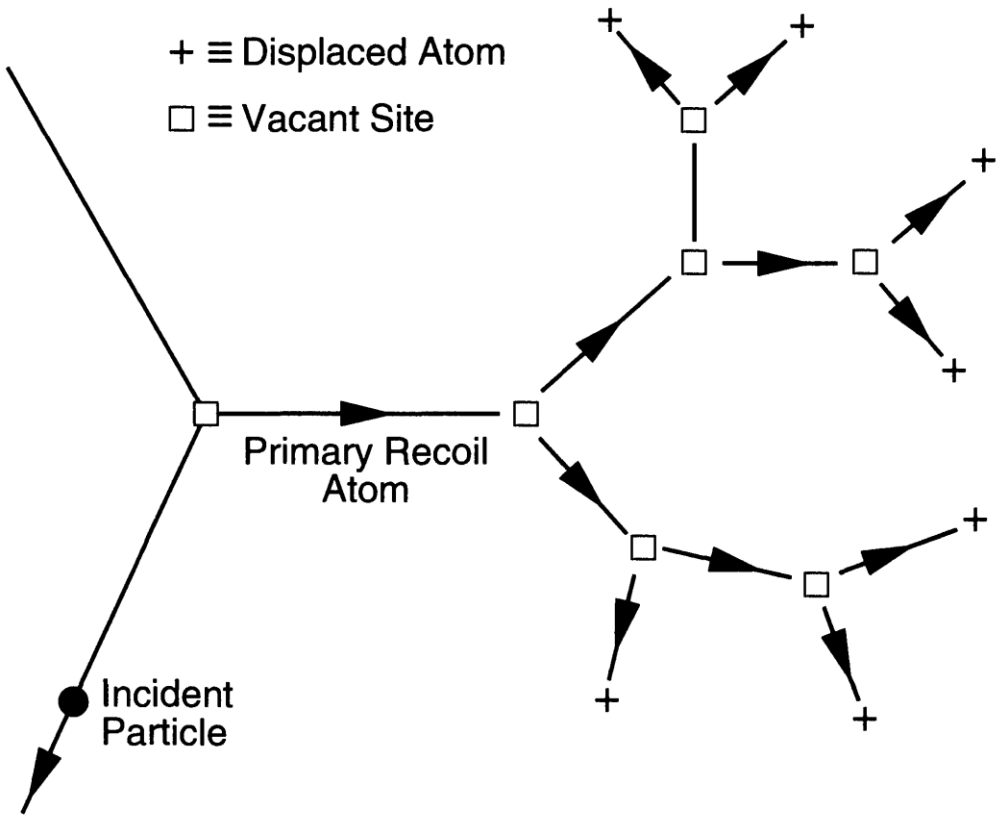

Figure 2. Schematic of the formation of collision cascade by primary knock-on atom (PKA). [13]

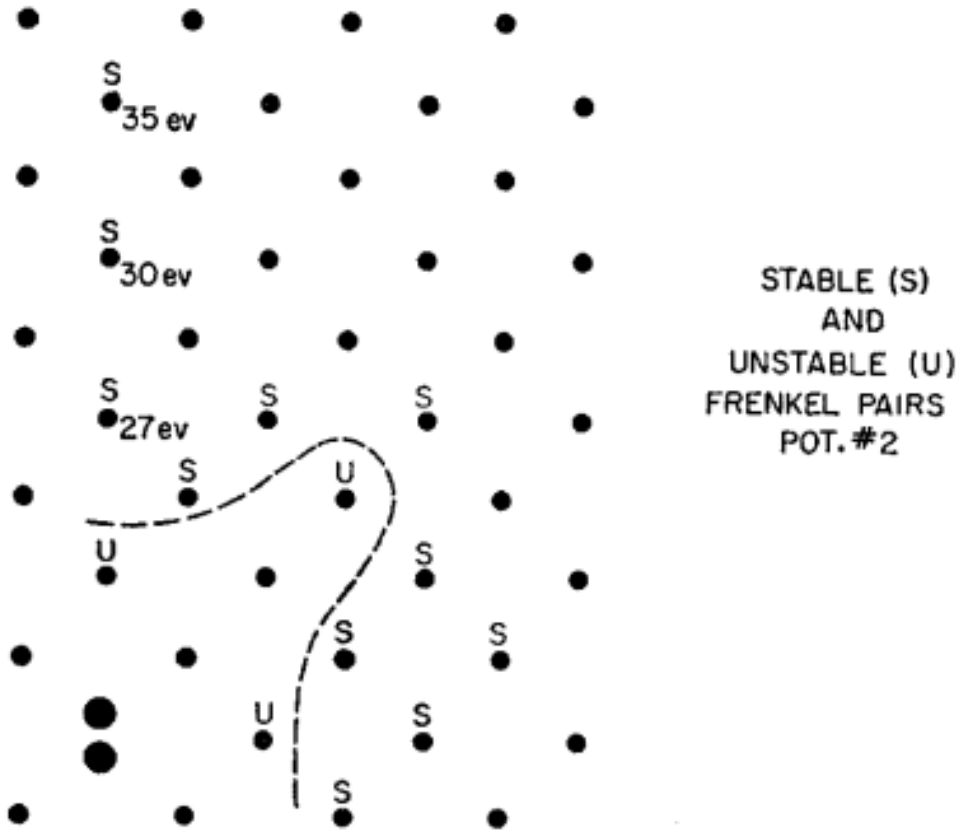

Figure 3. Stability of Frenkel pairs in {100} plane of copper. Dotted lines separates stable from unstable sites for a vacancy. Approximate threshold energies for dynamic production of three particular pairs are indicated. [16]

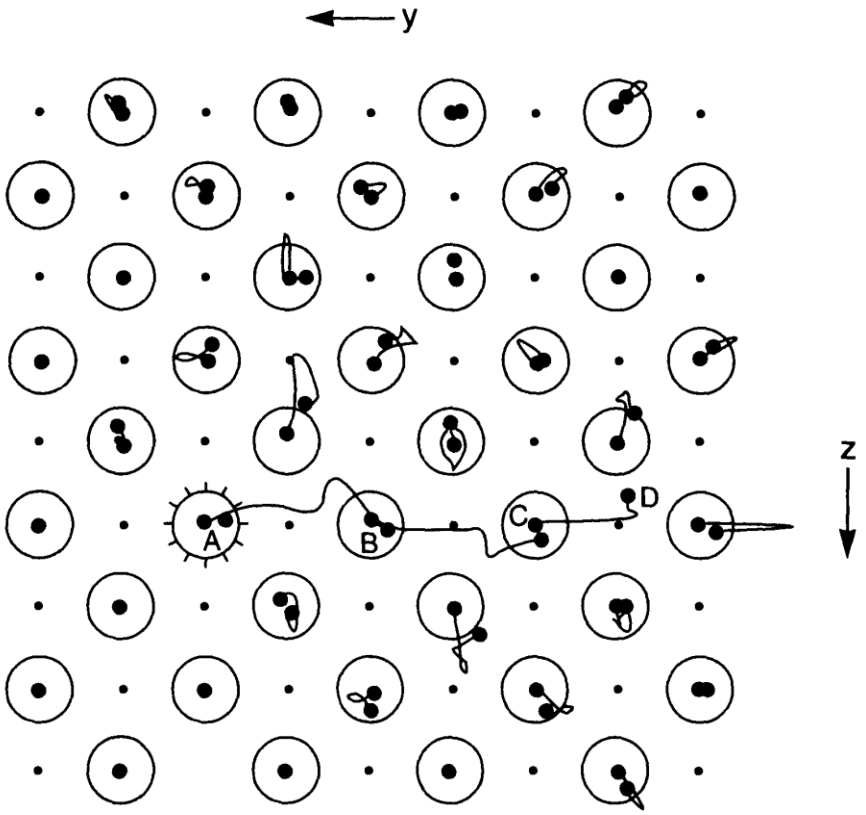

Figure 4. The atomic orbits of lattice atoms produced by a 40 eV PKA in (100) plane of an FCC crystal. The PKA produced at lattice site A, created a vacancy at A, replacements at B and C, and a split interstitial at D. [16]

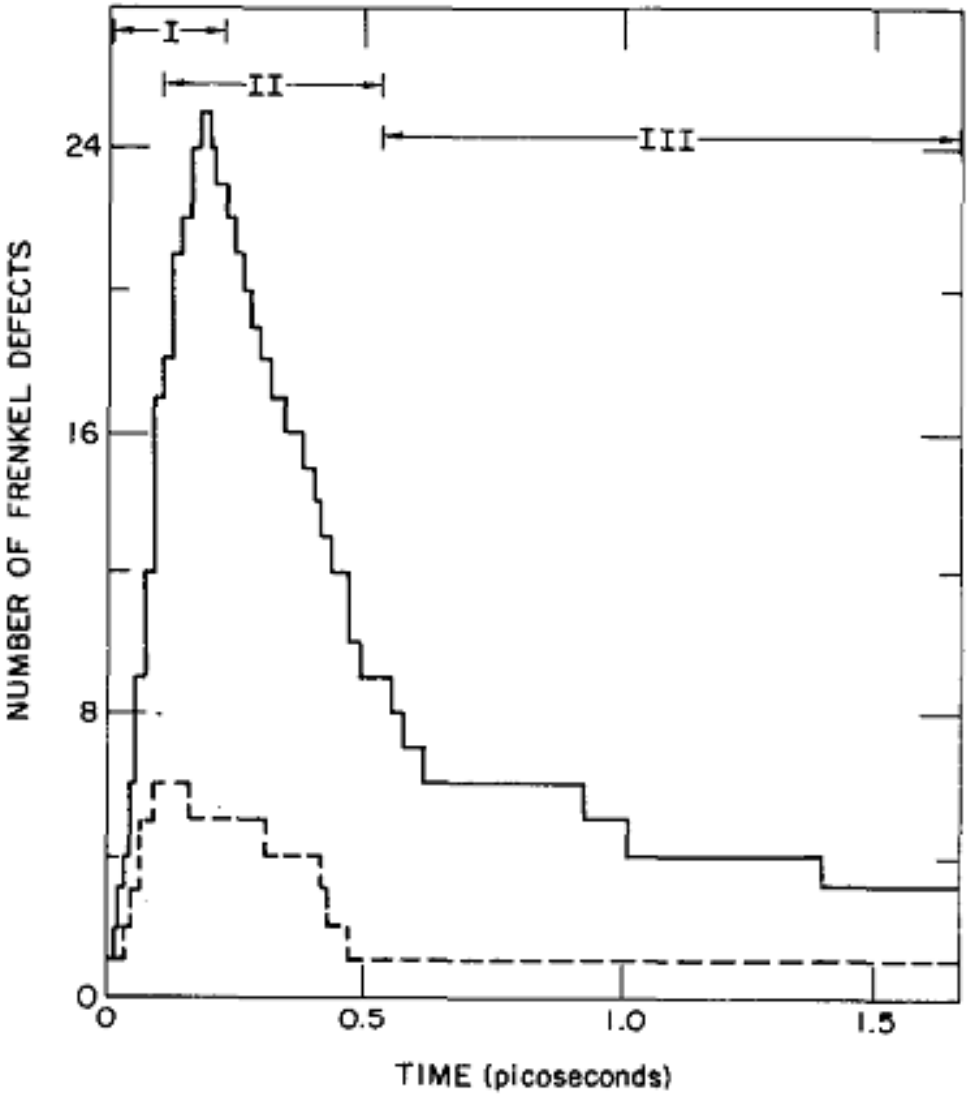

Figure 5. Time development of Frenkel pair concentrations calculated for cascades of two different energies: 600 eV (- - - -) and 2.5 keV (------) in Tungsten. [18]

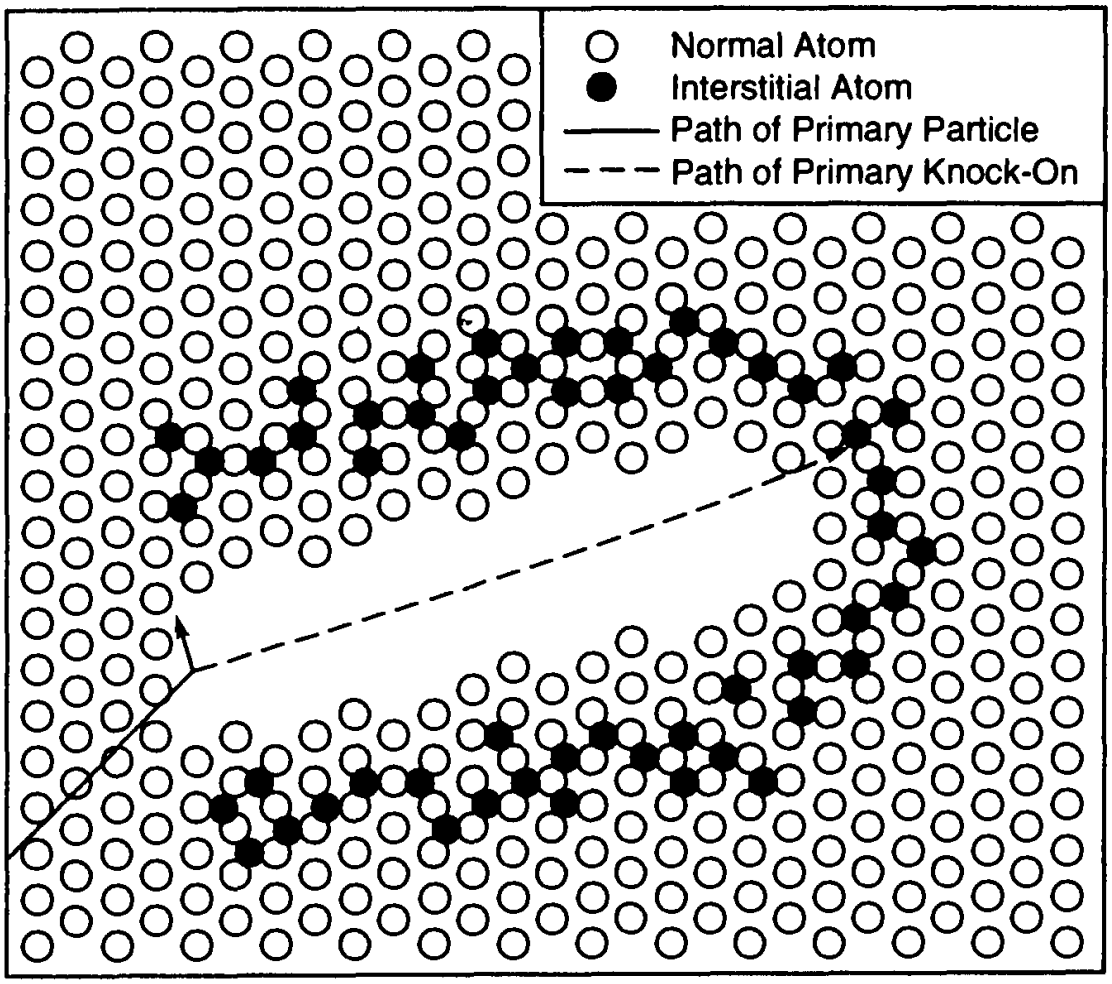

Figure 6. Schematic of a highly damaged volume of material when the mean free path between collisions approaches the atomic spacing of the target atoms. [21]

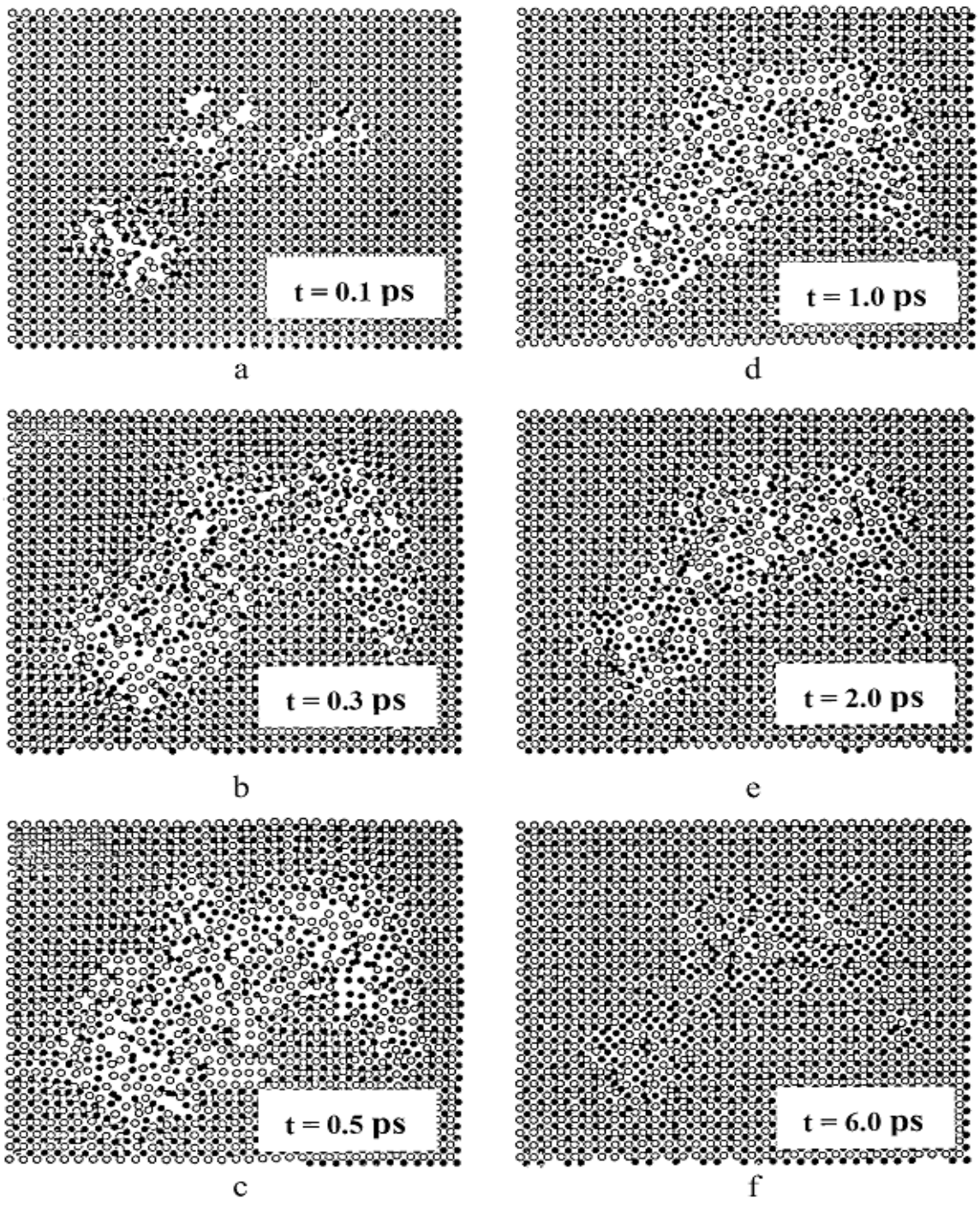

Figure 7. Position of atoms in a cross-sectional slice, one lattice parameter thick during a 10-keV event in β-NiAl. [22]

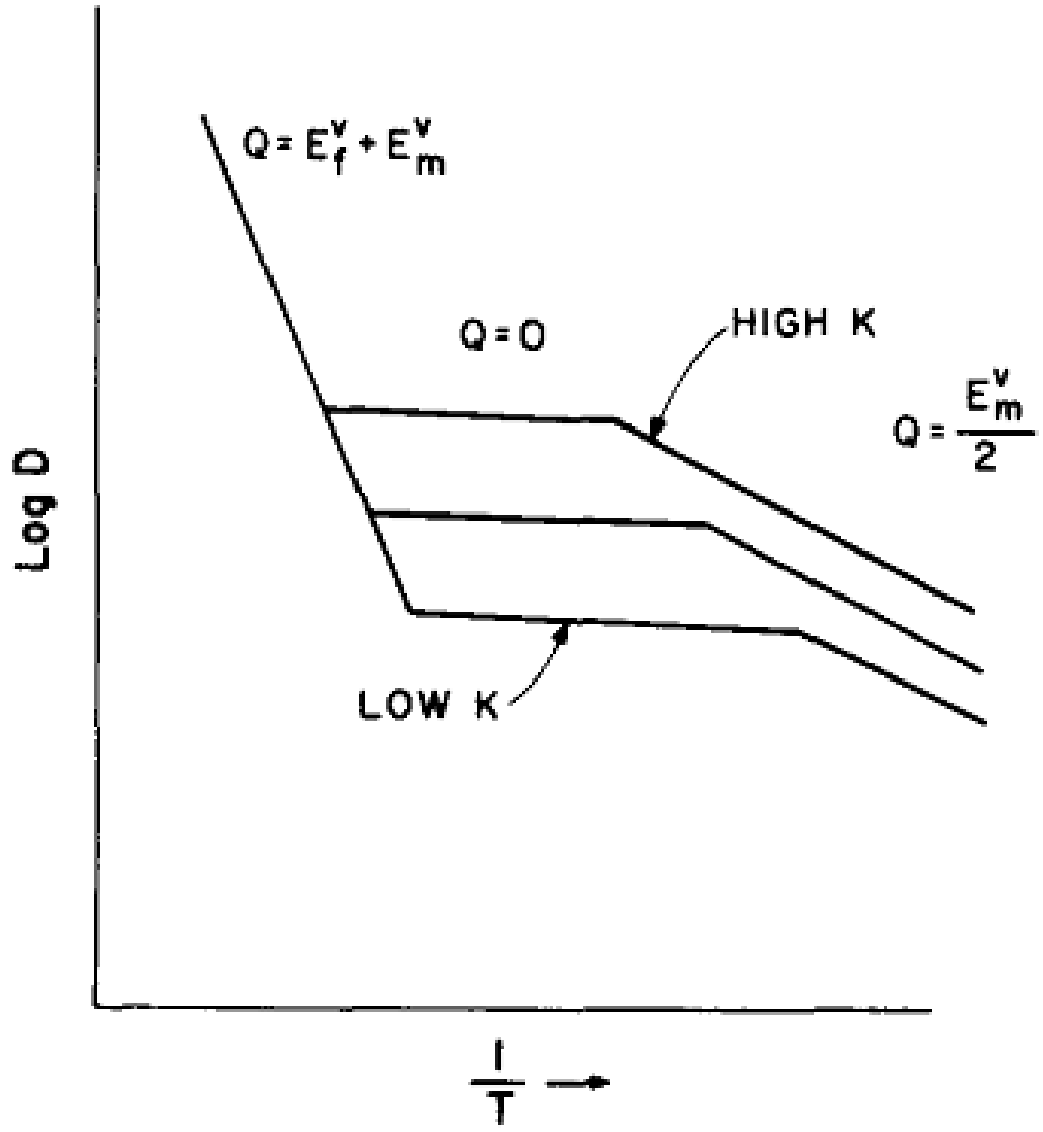

Figure 8. Schematic plot of different regimes for diffusion coefficient in irradiated metal at different displacement rates. [24]

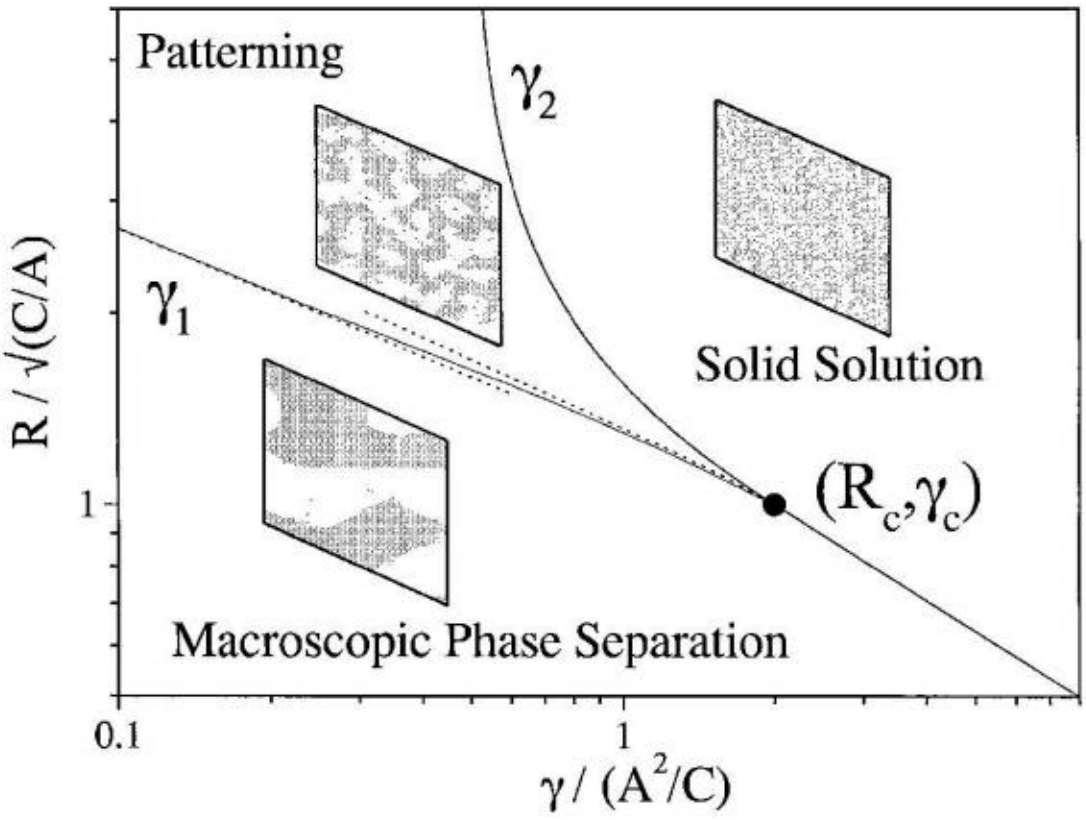

Figure 9. The Steady-state dynamic phase diagram for a model A-B alloy as a function of relocation distance, *R* and reduced rate of ballistic mixing, γ. [8]

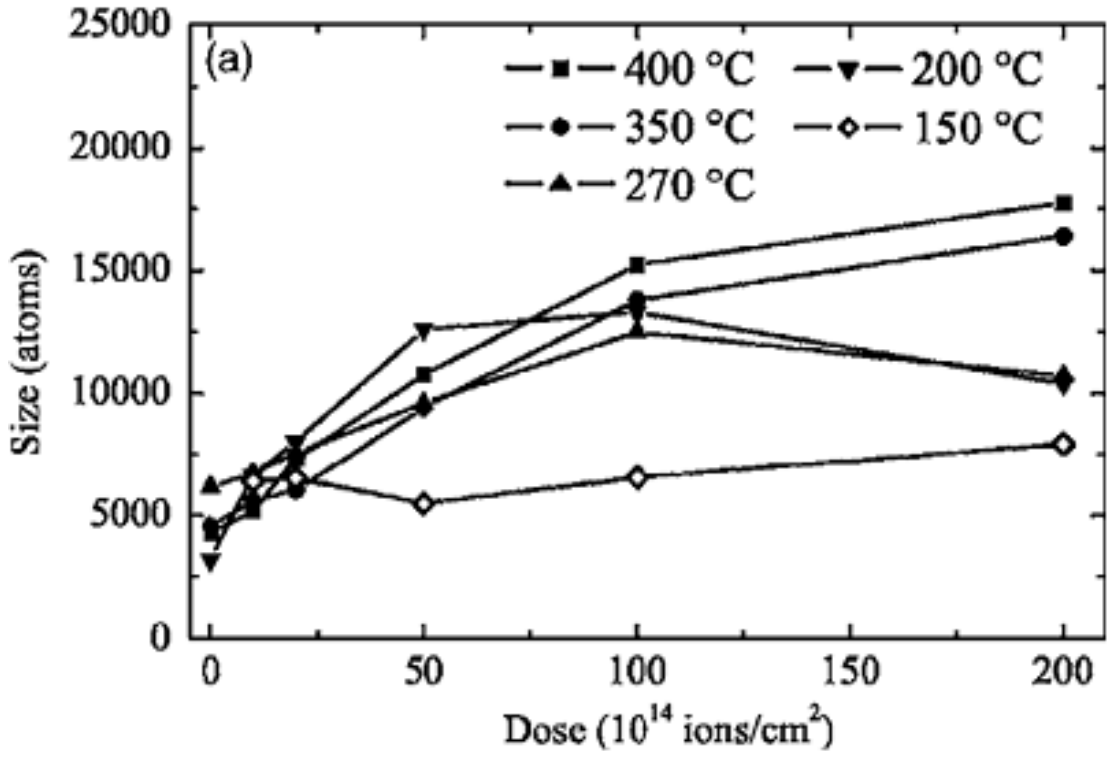

Figure 10. Dependence of particle size as a function of irradiation dose for pre-irradiated $Cu_{85}Co_{15}$ samples. [9]

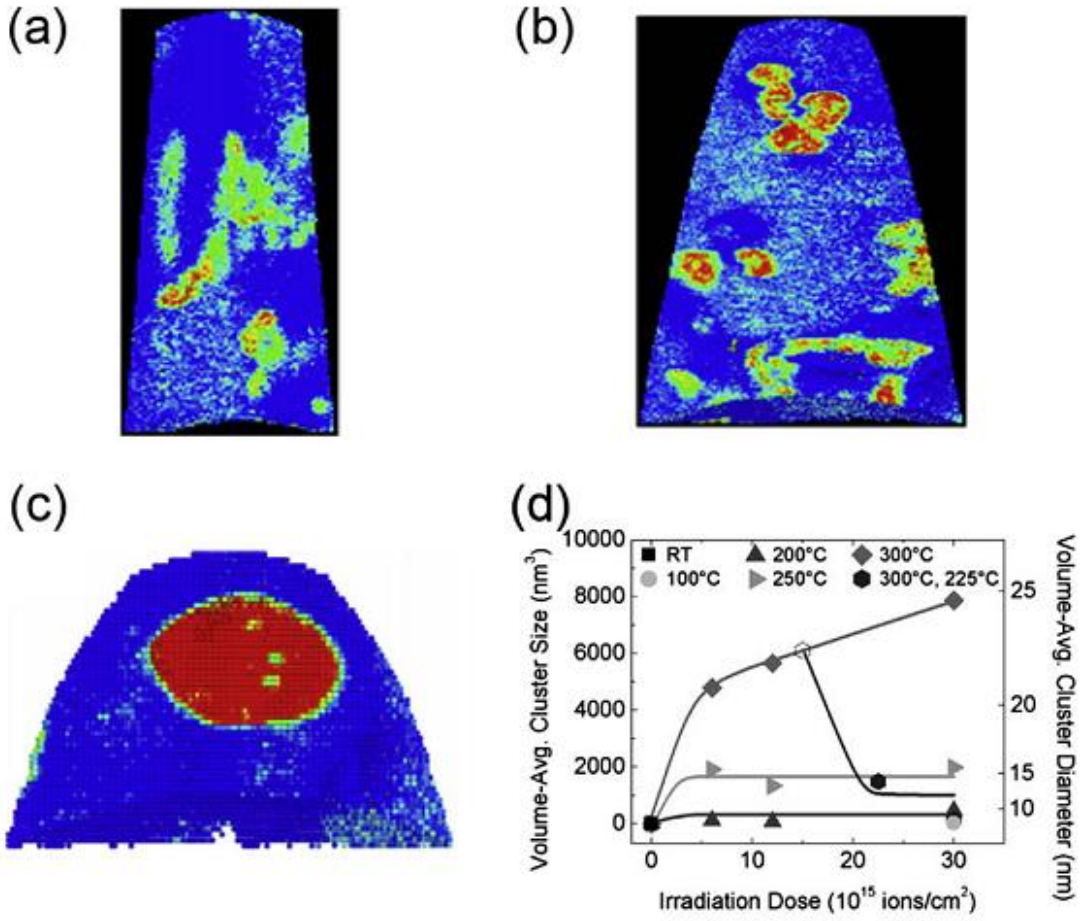

Figure 11. APT results of irradiation induced precipitation of Fe in Cu. Volume averaged size of Fe precipitates in Cu as a function of dose during irradiation at different temperatures showing patterning regime. Concentration maps of irradiate $Cu_{88}Fe_{12}$ at (a) 250 °C, (b) 300 °C, (c) 350 °C. Cluster size is plotted as a function of doze in (d). [10]

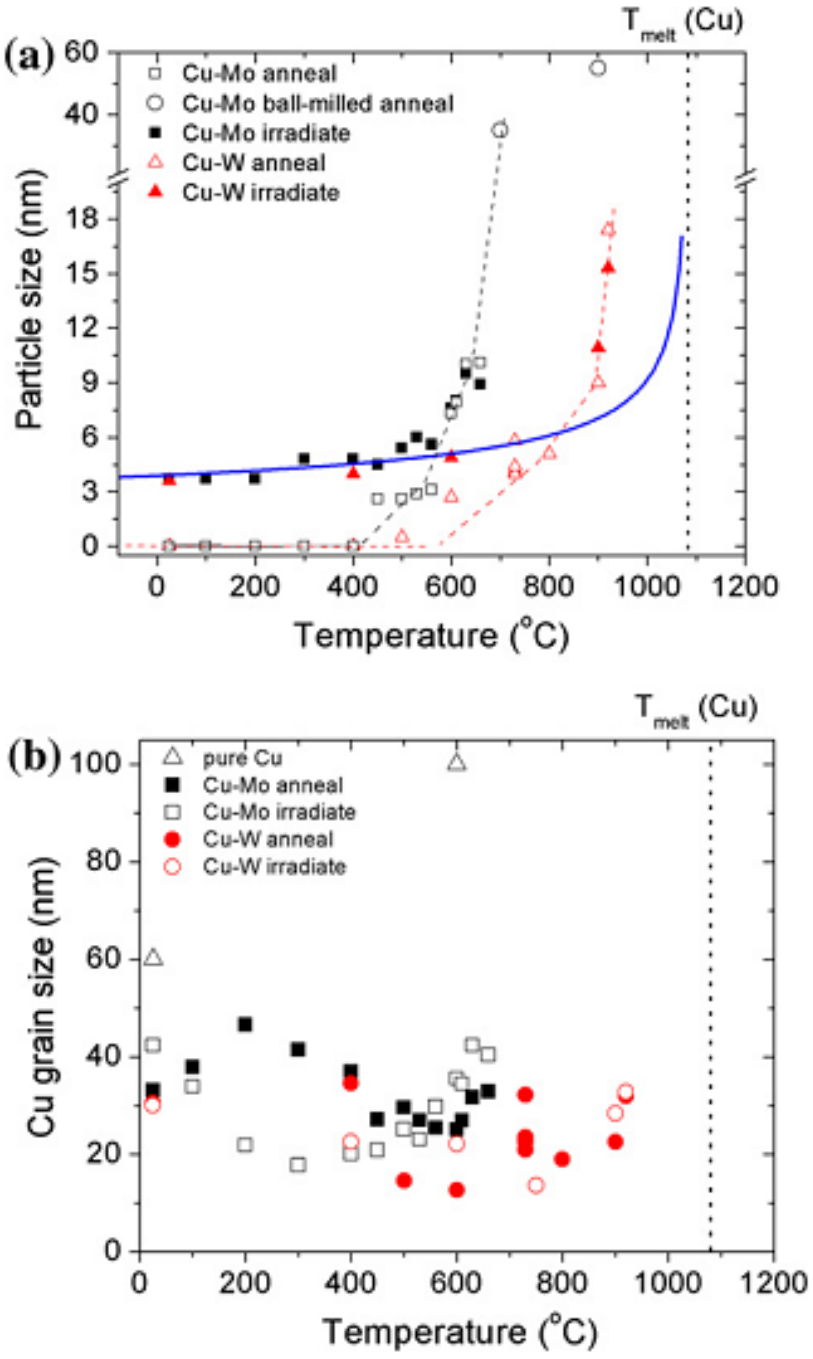

Figure 12. (a) Plot of precipitate size vs. temperature during thermal annealing and irradiation at high temperature in Cu-Mo and Cu-W alloys. (b) Plot of grain size vs. temperature during thermal annealing and irradiation at high temperature in Cu-Mo and Cu-W alloys. [11]

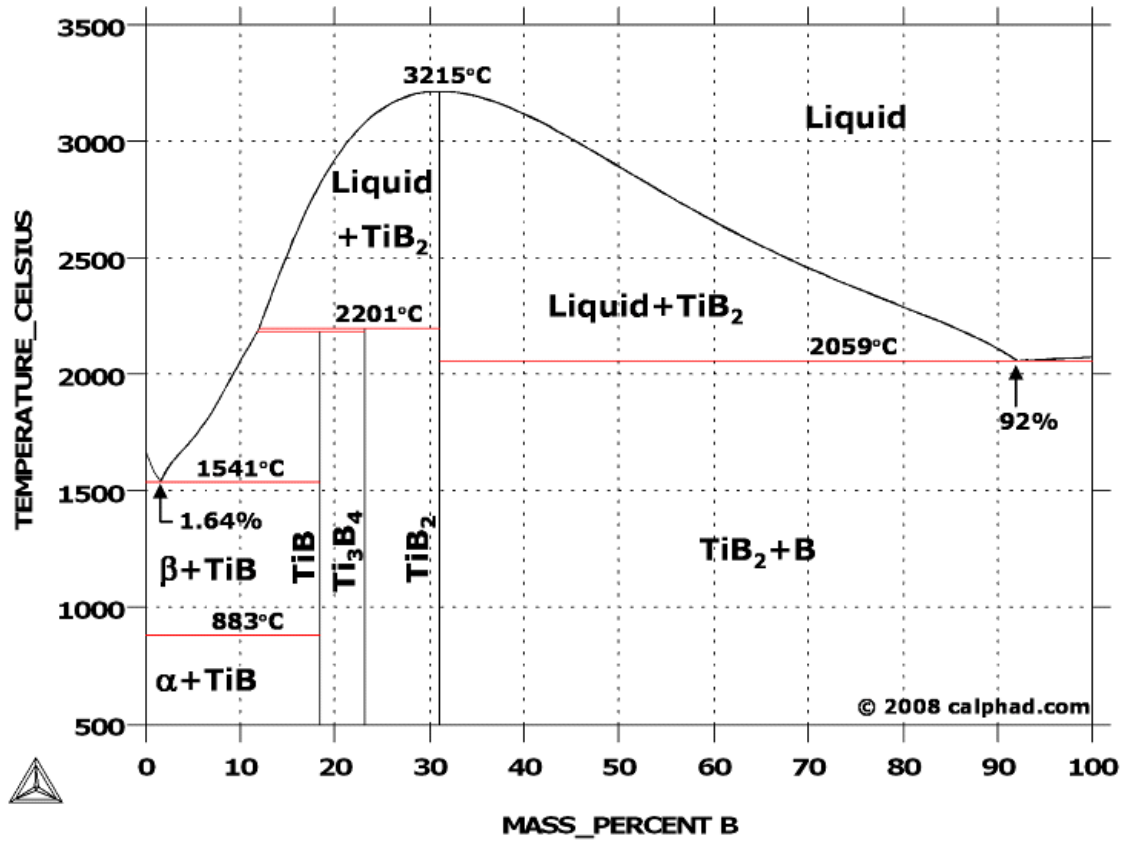

Figure 13. A binary phase diagram of Ti-B calculated with Thermo-Calc, coupled with SSOL4 thermodynamic database. [32]

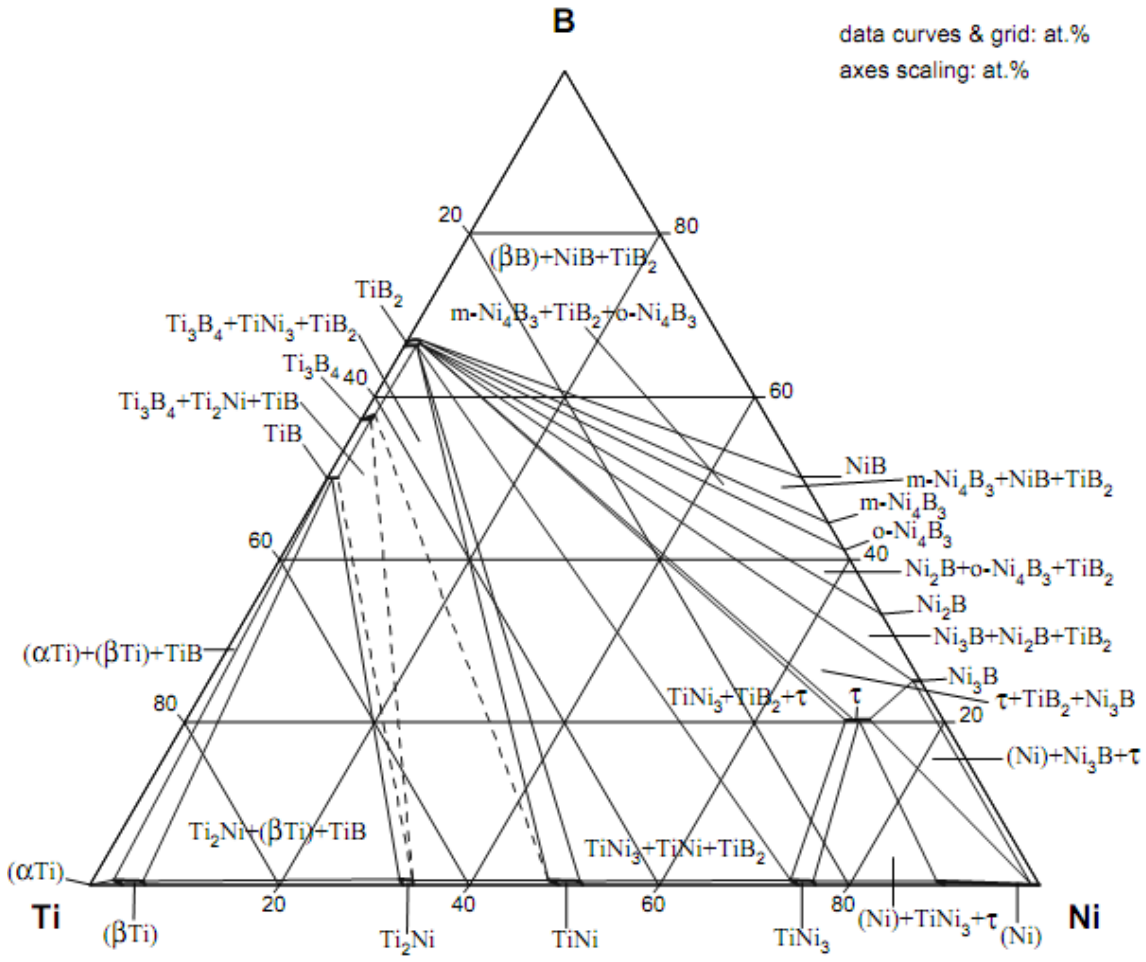

Figure 14. Isothermal section of Ni-T-iB phase diagram at 800 °C. [33]

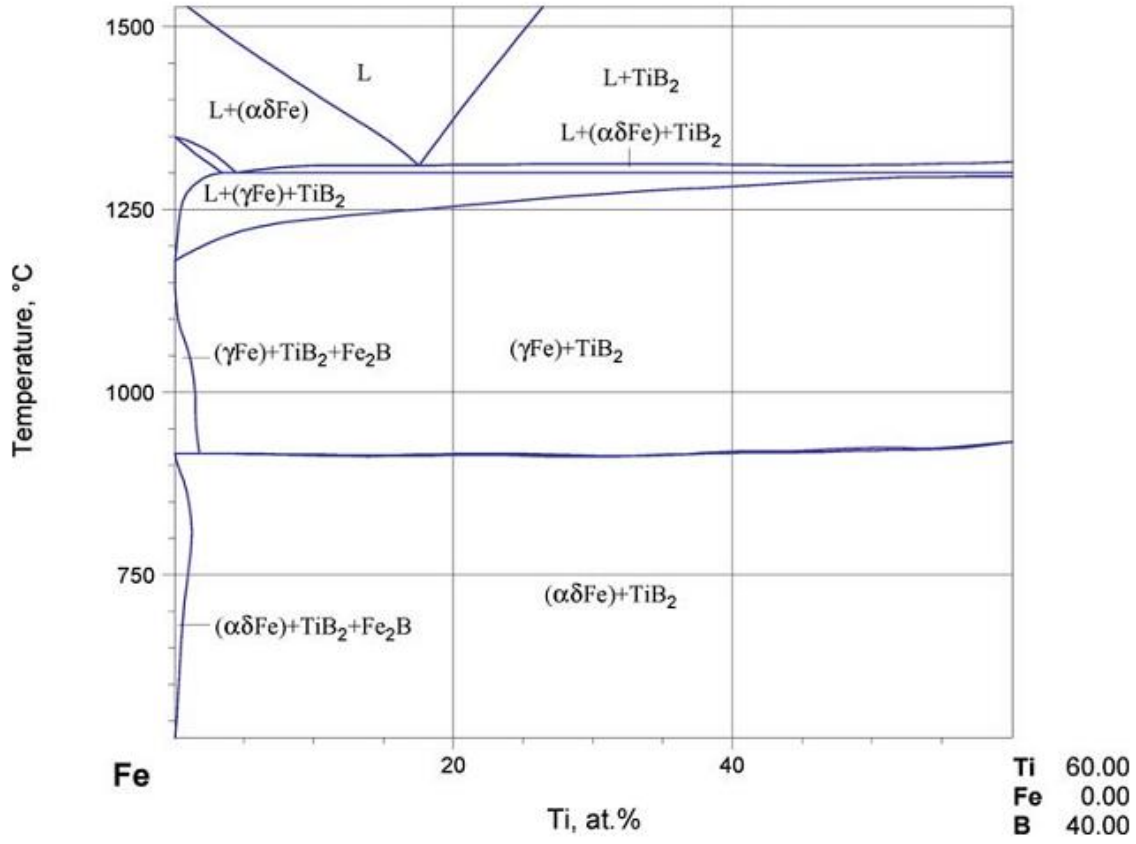

Figure 15. A pseudo binary phase diagram of Fe-TiB_2. [33]

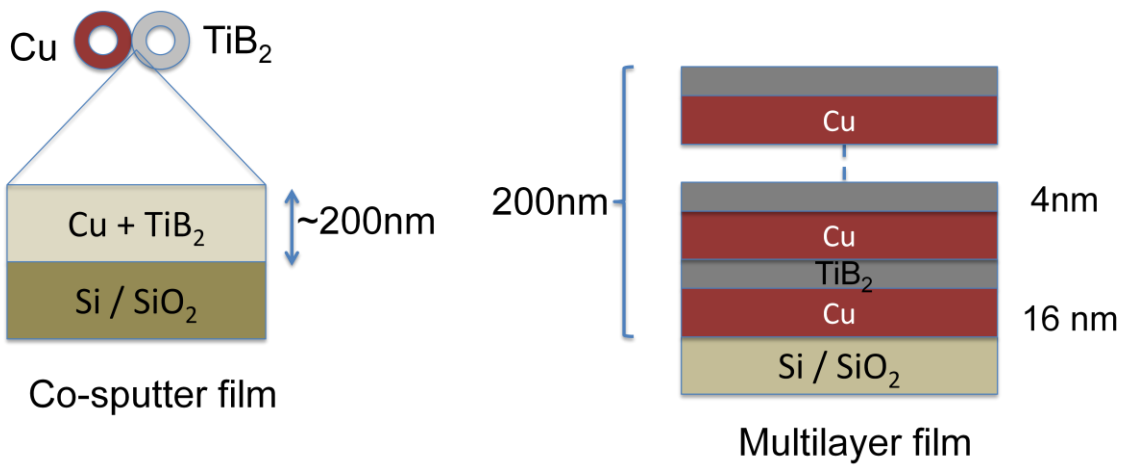

Figure 16. Schematic illustration of the different types of samples used.

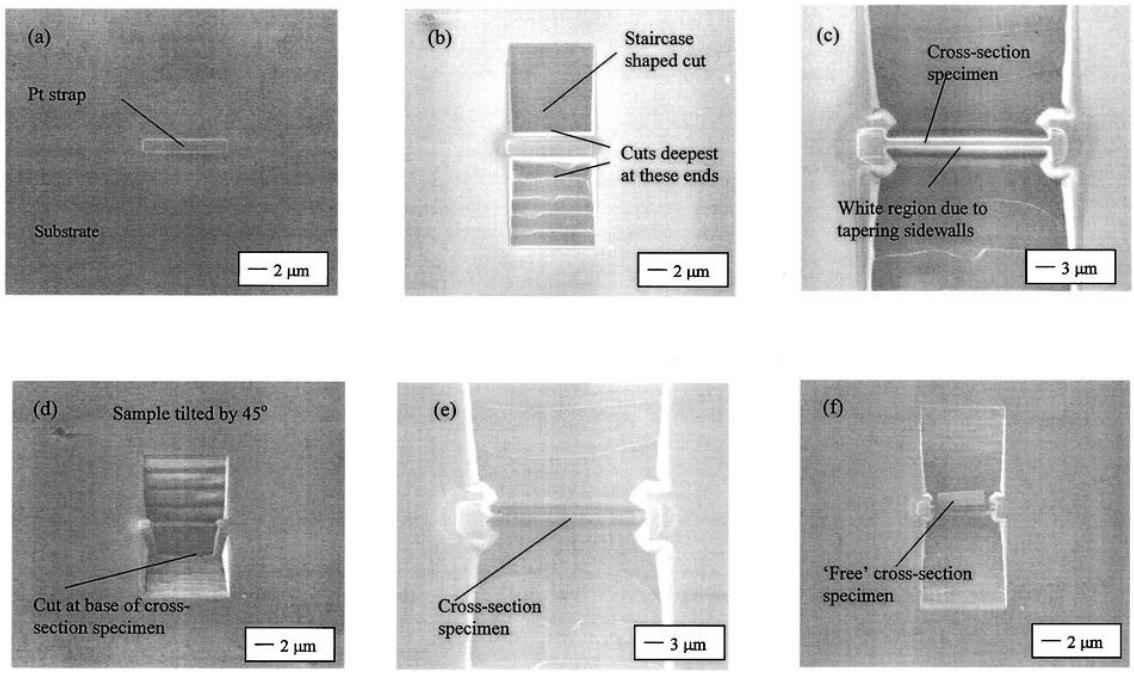

Figure 17. Preparation of a cross-section specimen by the liftout technique, (a) deposition of a platinum strip over the region of interest, (b) staircase cuts, (c) thinning of the cross-section to about 500 nm, (d) making a U-cut, (e) further thinning of the sample until about 70 nm, (f) cutting the edges and liftout. [36]

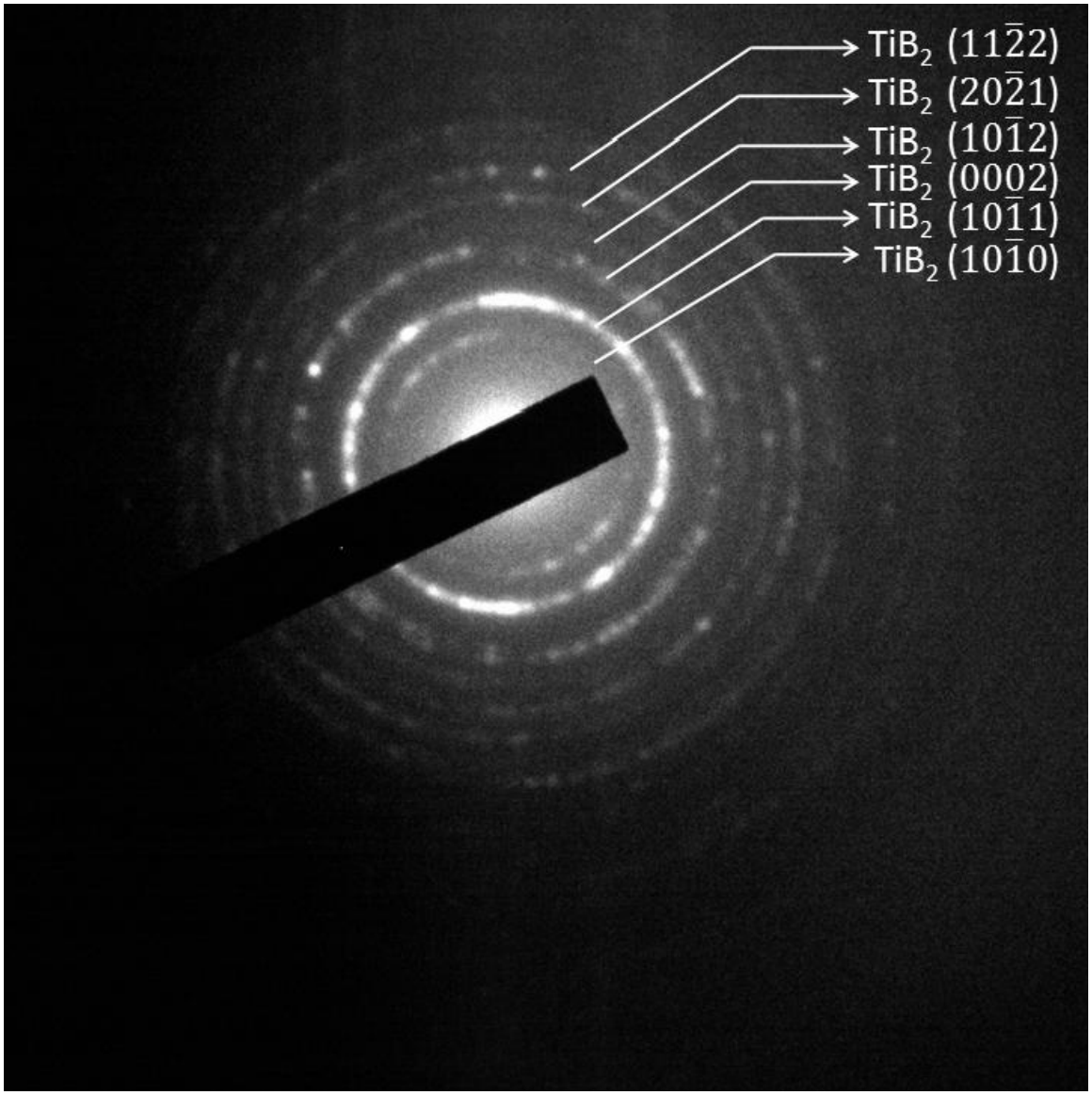

Figure 18. Electron diffraction pattern of pure TiB_2 thin film, irradiated with a dose of 3×10^{16} ions/ cm^{-2} at 800 °C. All the reflections of crystalline hexagonal TiB_2 are indexed.

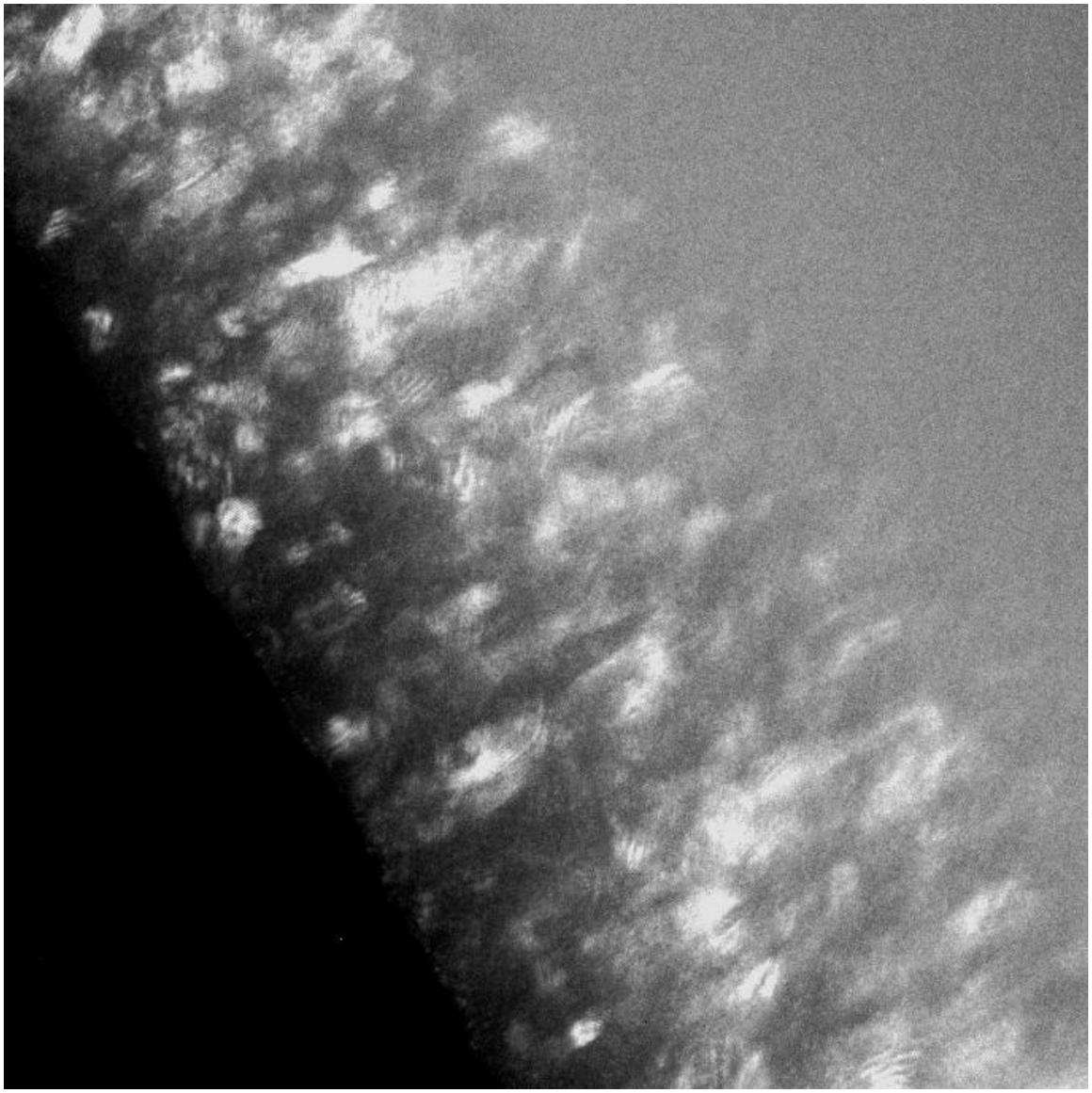

Figure 19. Dark Field imaging of irradiated TiB_2 thin film sample with Kr^+ ions at a dose of 3×10^{16} ions/ cm^{-2} at 800 °C.

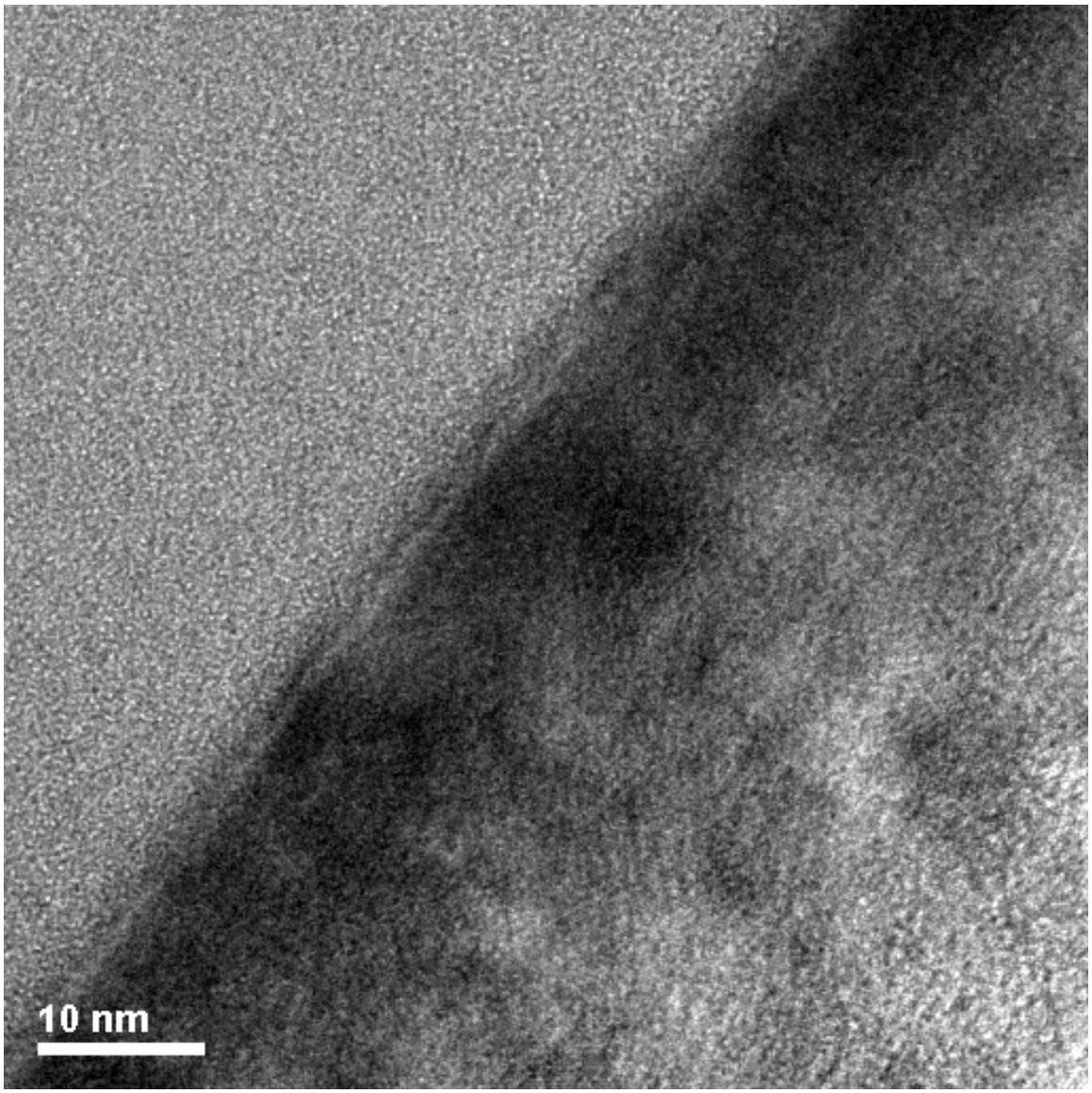

Figure 20. A Bright Field image of irradiated TiB_2 thin film at 800 °C. TiB_2 particles can be seen.

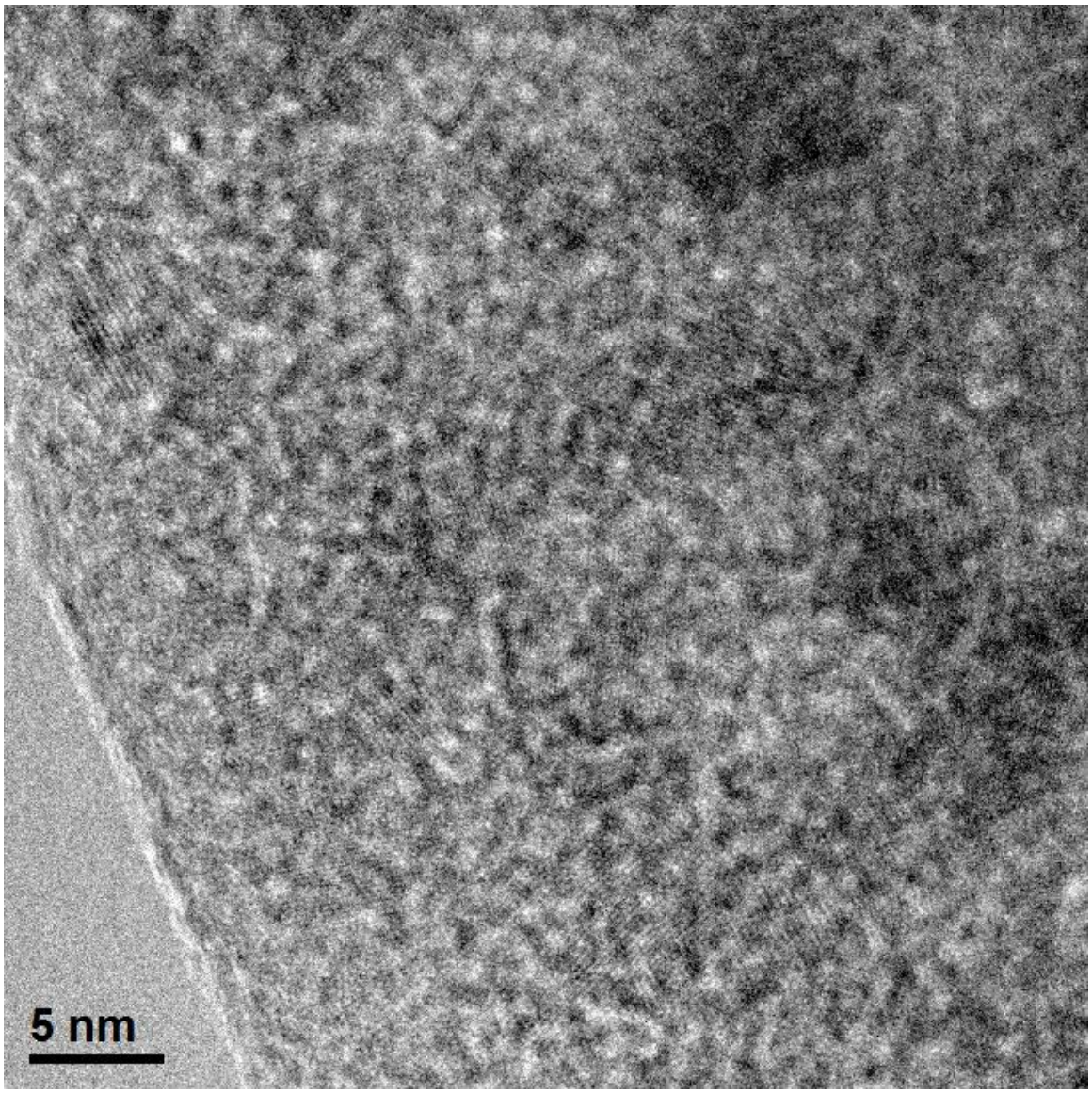

Figure 21. A High Resolution Electron Micrograph (HREM) of pure TiB_2 film irradiated with Kr^+ ions at 800 °C for 1 hour creating about 75 dpa.

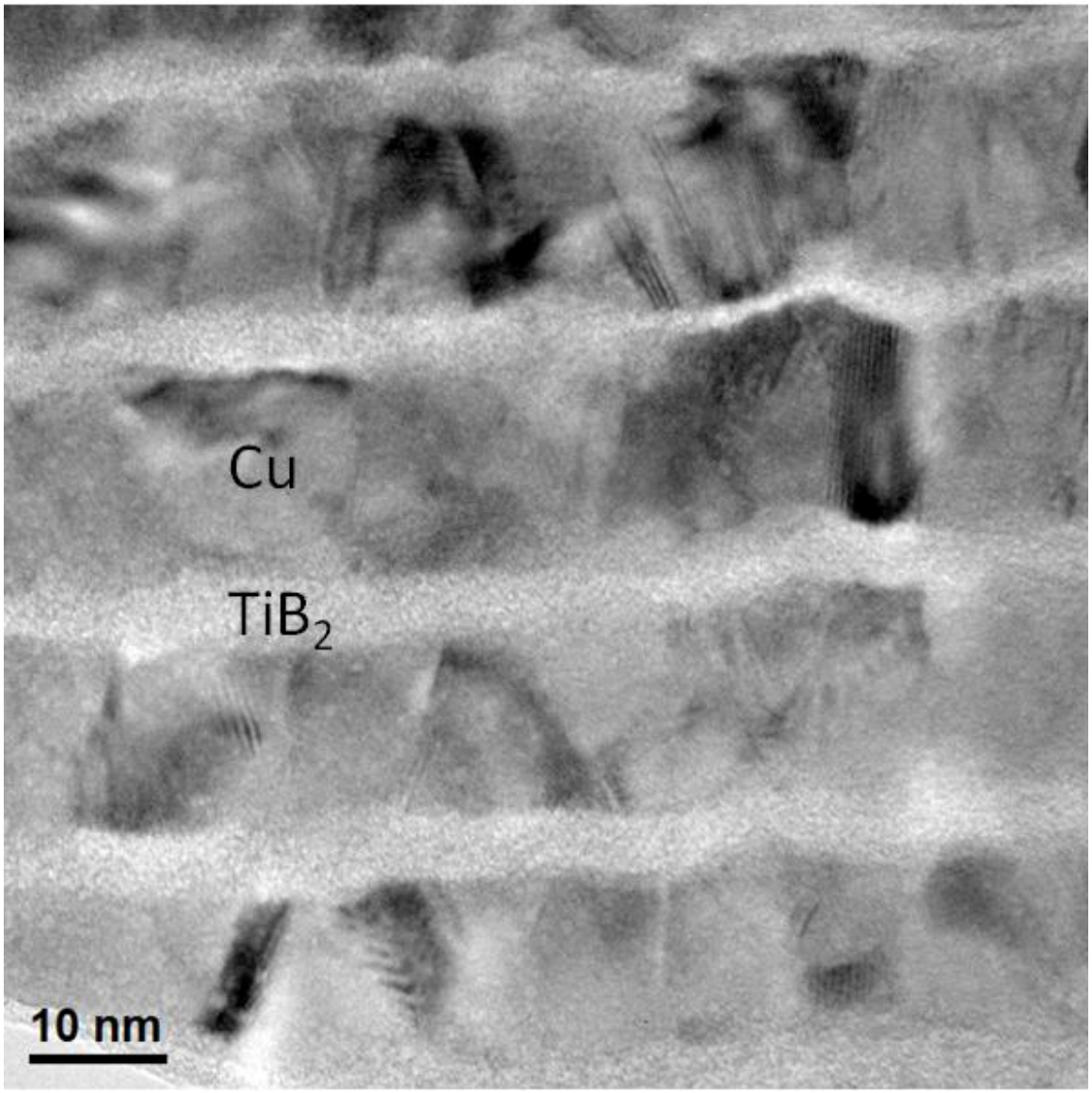

Figure 22. A Bright Field image of as grown multilayer Cu/ TiB_2 thin film sample. Alternate layers of crystalline Cu and amorphous TiB_2.

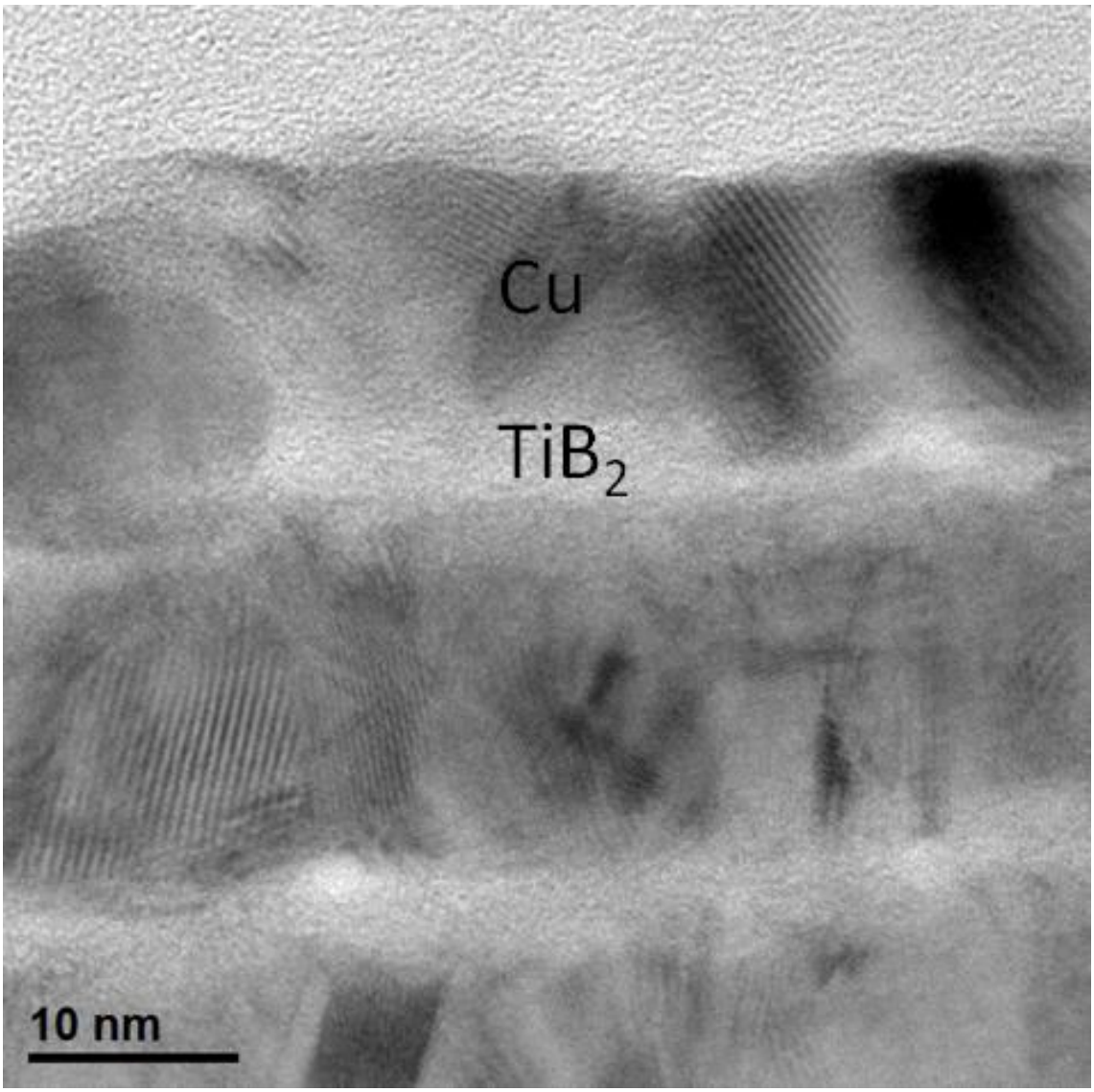

Figure 23. A high resolution electron microscopy image of as-grown multilayer Cu/TiB_2 sample showing nanoscale twinning and surface roughness.

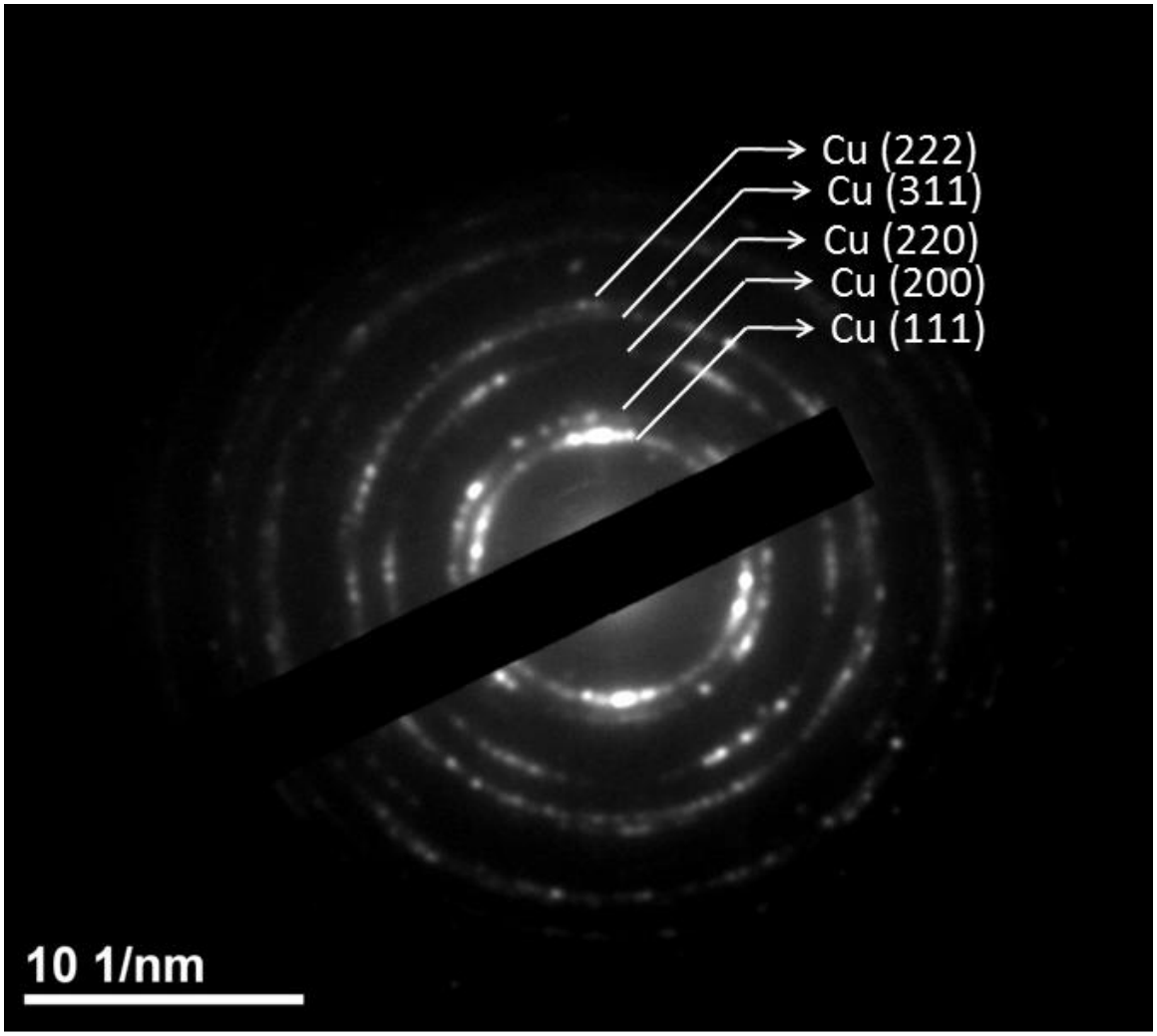

Figure 24. A electron diffraction pattern of as-grown multilayered Cu/TiB_2 thin film sample. Reflections for FCC Cu are indexed and no reflections of TiB_2 were observed.

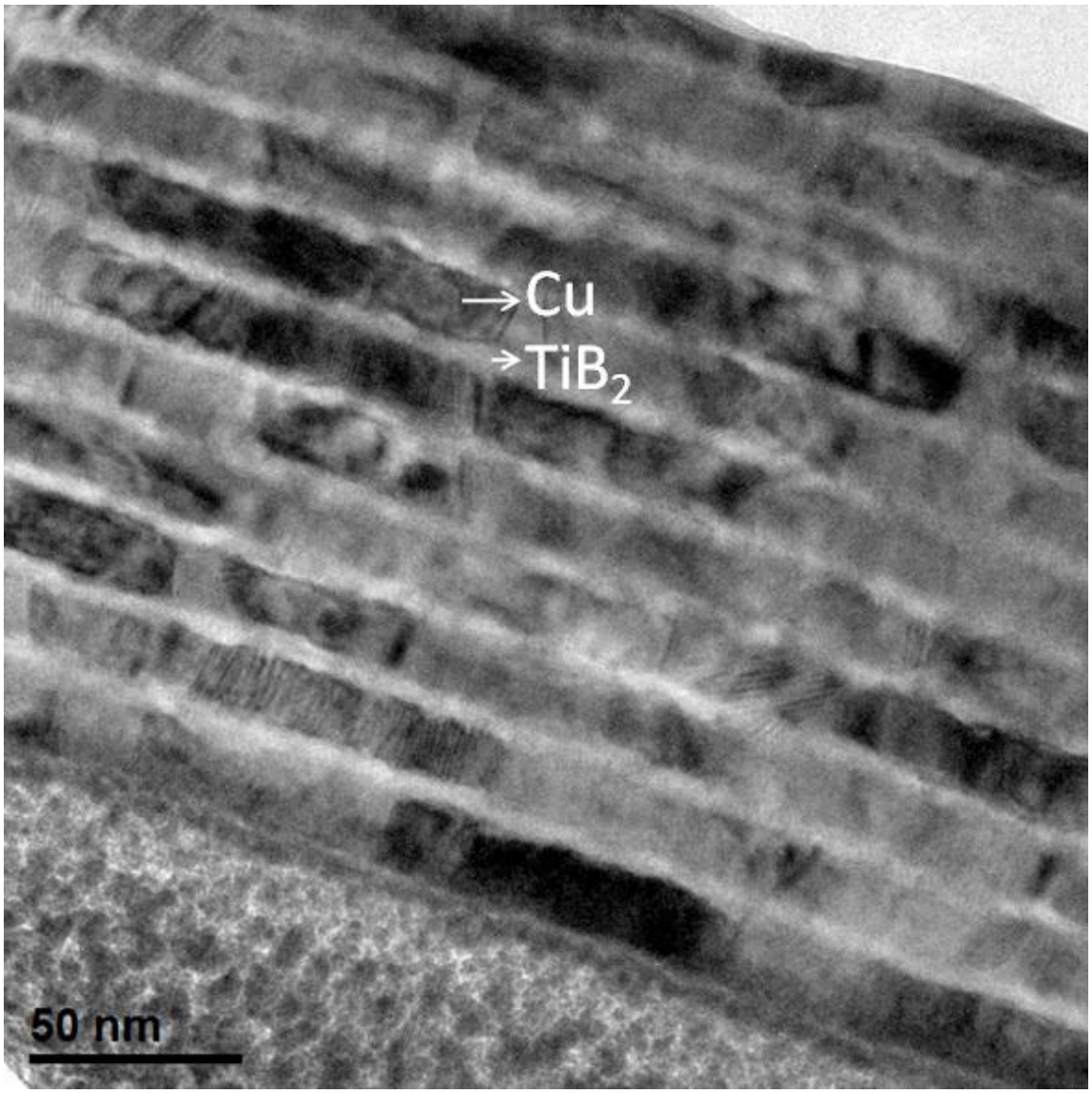

Figure 25. A Bright Field image of irradiated multilayer Cu/ TiB_2 thin film sample. Alternate layers of crystalline Cu and hexagonal, equilibrium phase TiB_2.

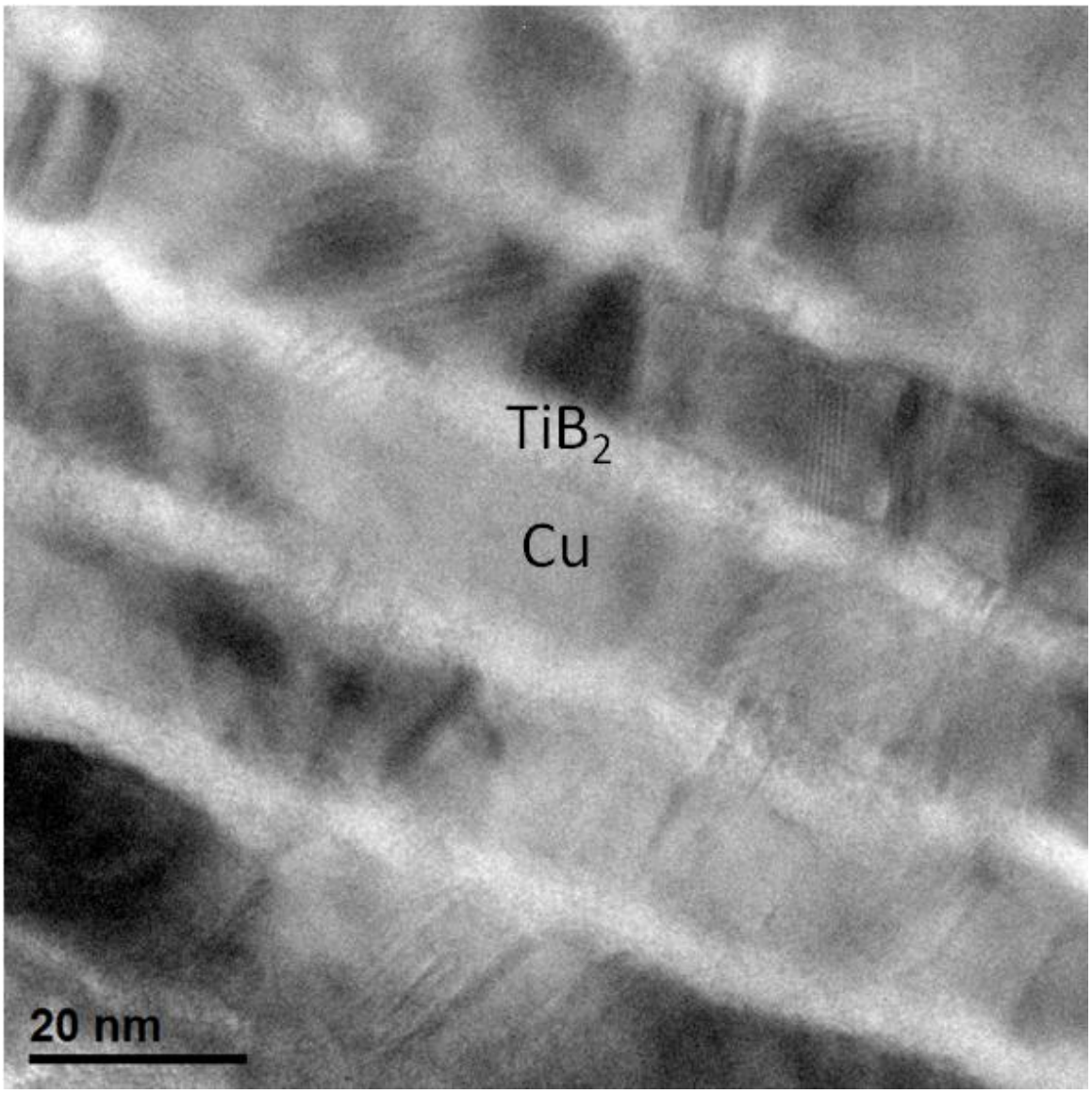

Figure 26. A high magnification image of the Cu/TiB_2 multilayers irradiated with Kr^+ ions at 650 °C.

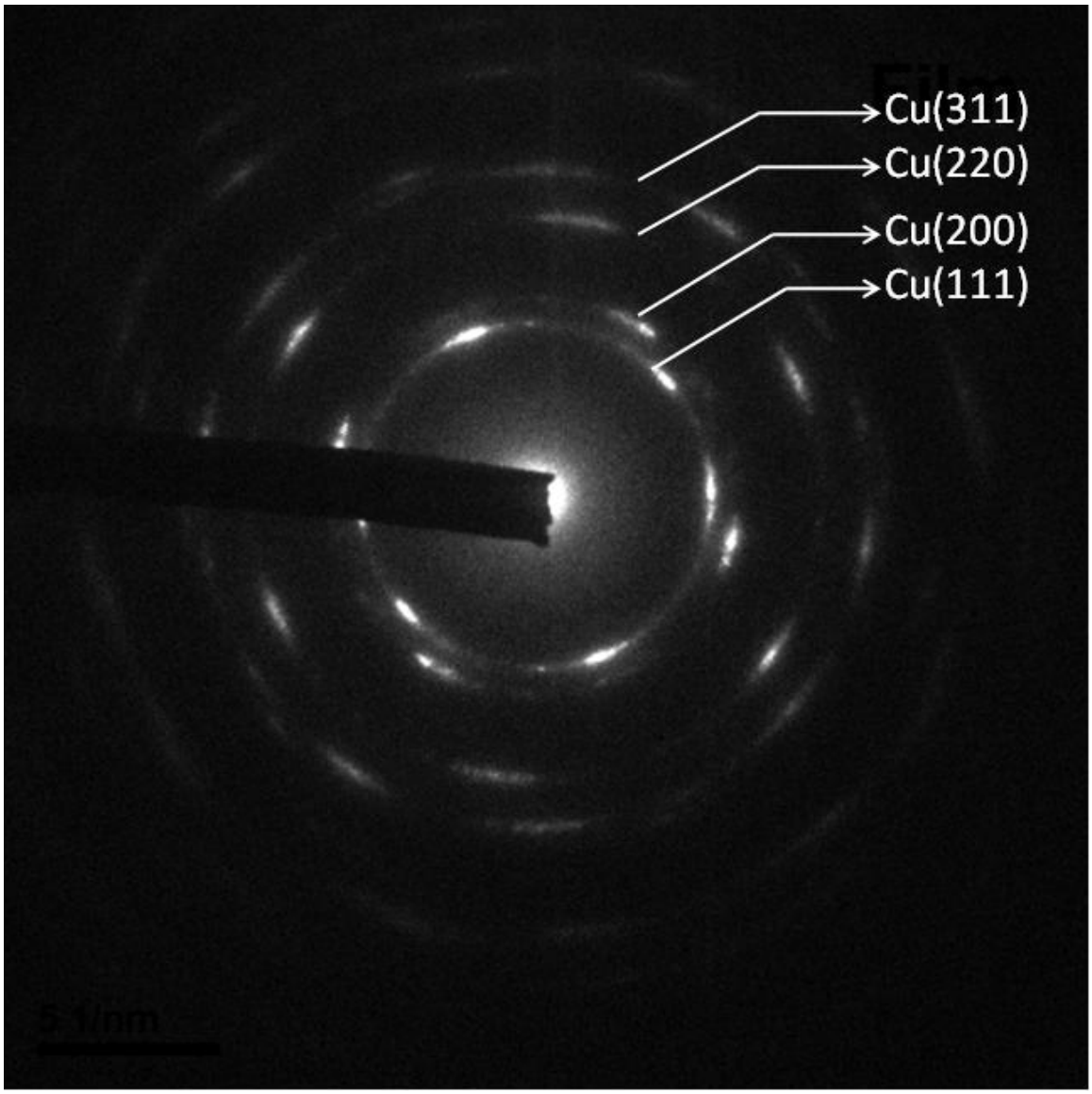

Figure 27. An electron diffraction pattern of as grown $Cu_{0.85}(TiB_2)_{0.15}$ thin film clearly showing only Cu FCC reflections.

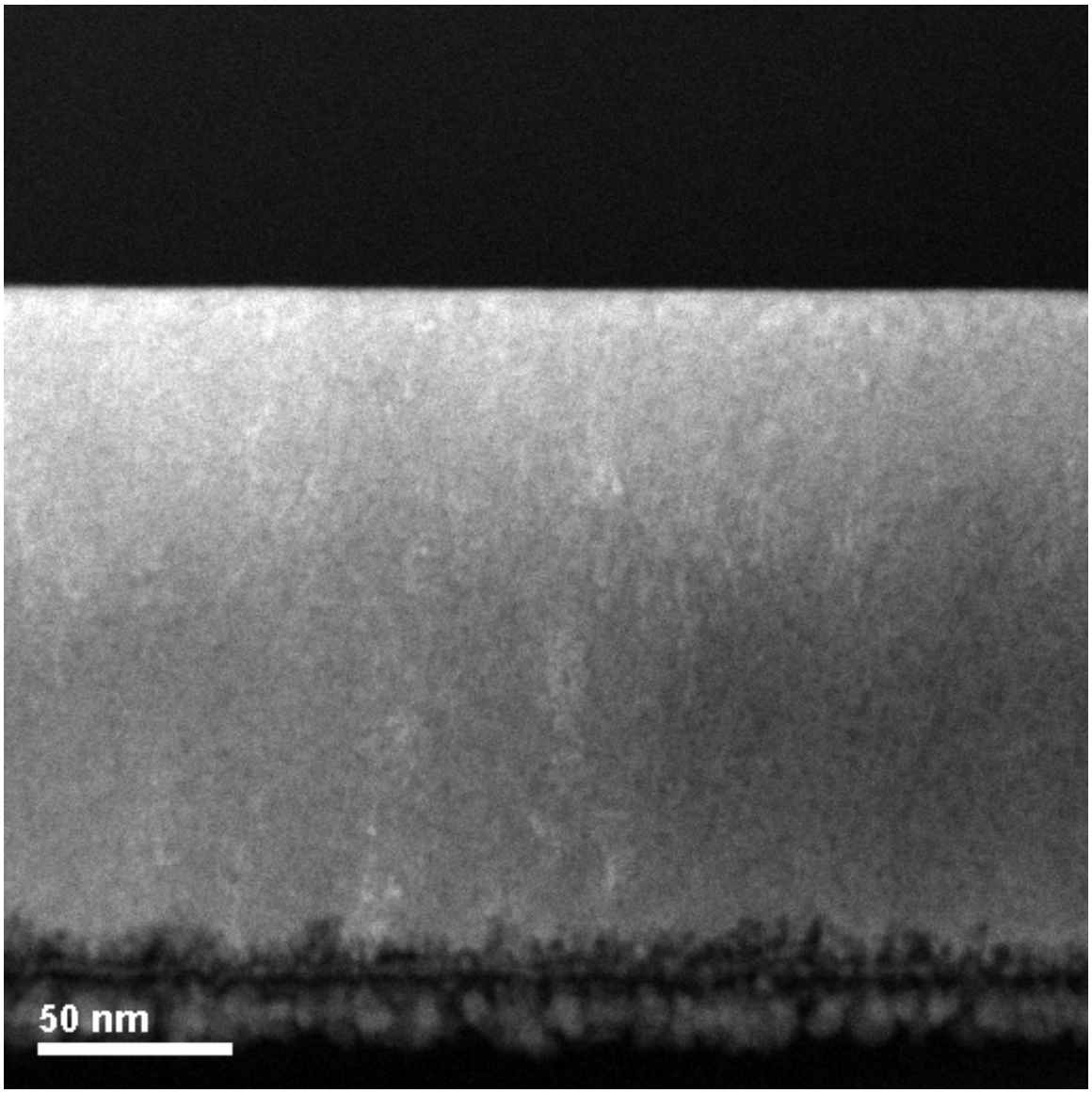

Figure 28. A HAADF image of as-grown single layer Co-sputtered $Cu_{0.85}(TiB_2)_{0.15}$.

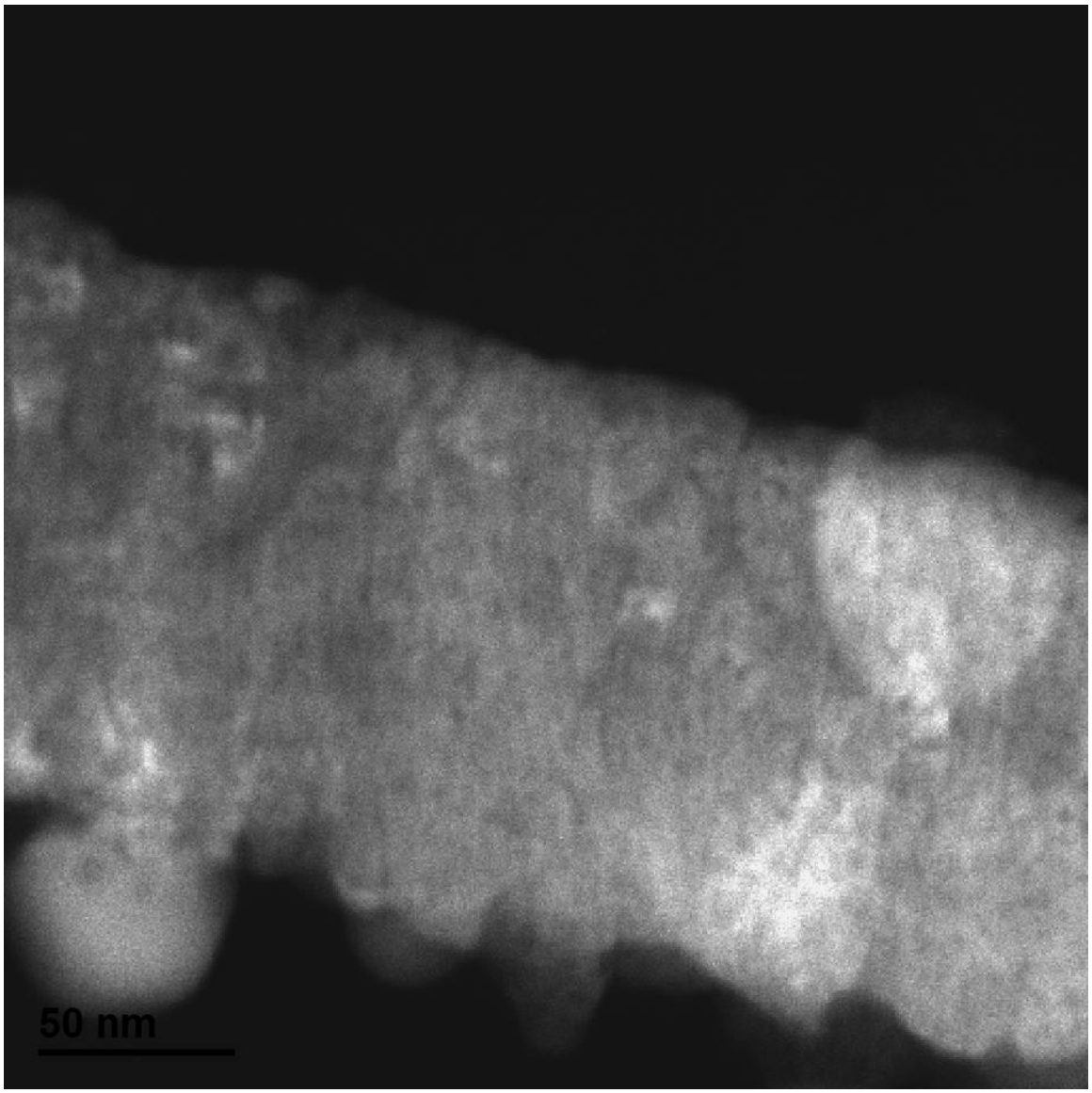

Figure 29. A HAADF image of a co-sputtered sample irradiated at room temperature with 3×10^{16} ions/ cm^{-2} Kr^{+} ions.

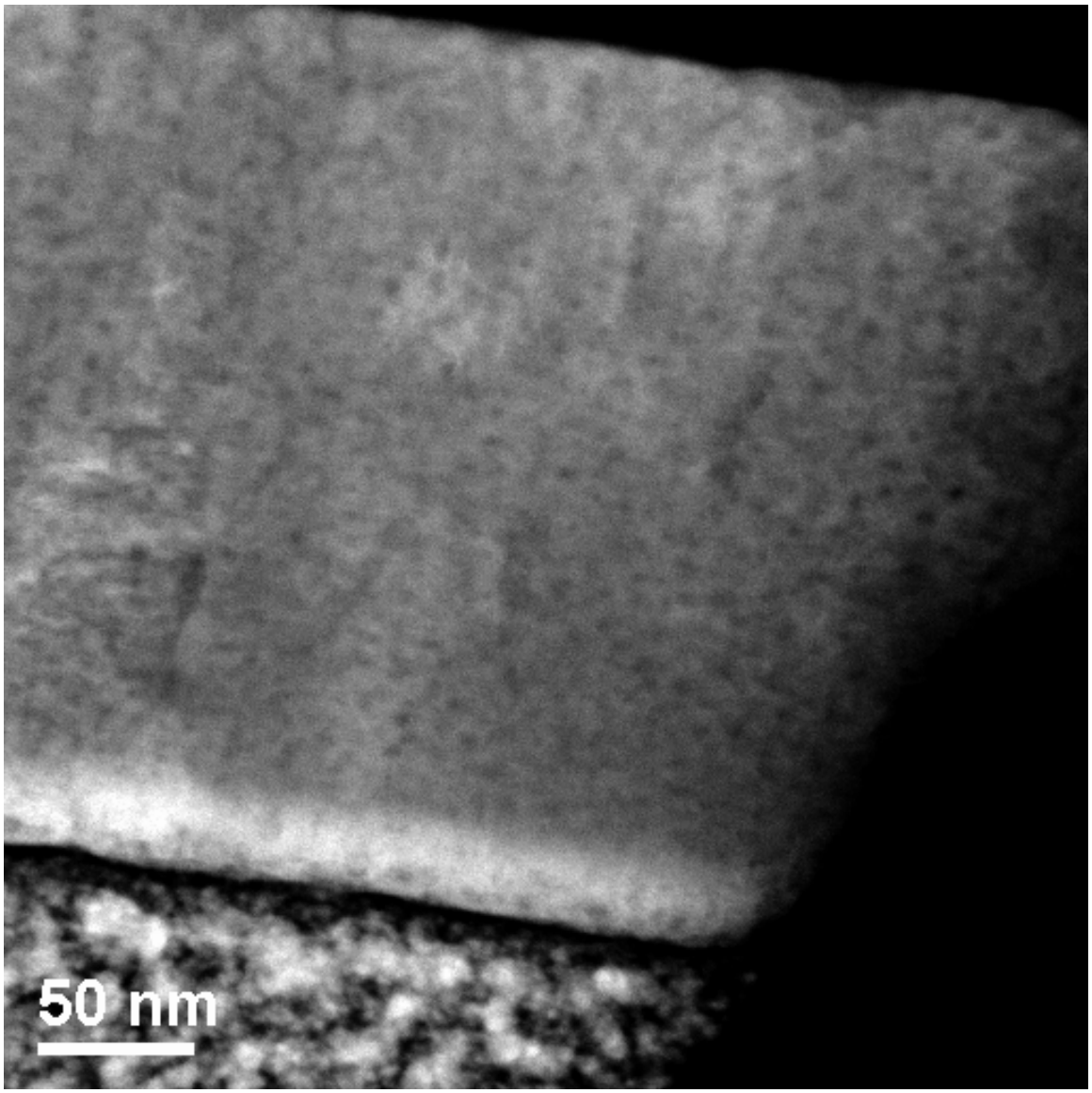

Figure 30. A HAADF image of a co-sputtered $Cu_{0.85}(TiB_2)_{0.15}$ film irradiated with a dose of 1×10^{16} ions/ cm^{-2} at 650 °C.

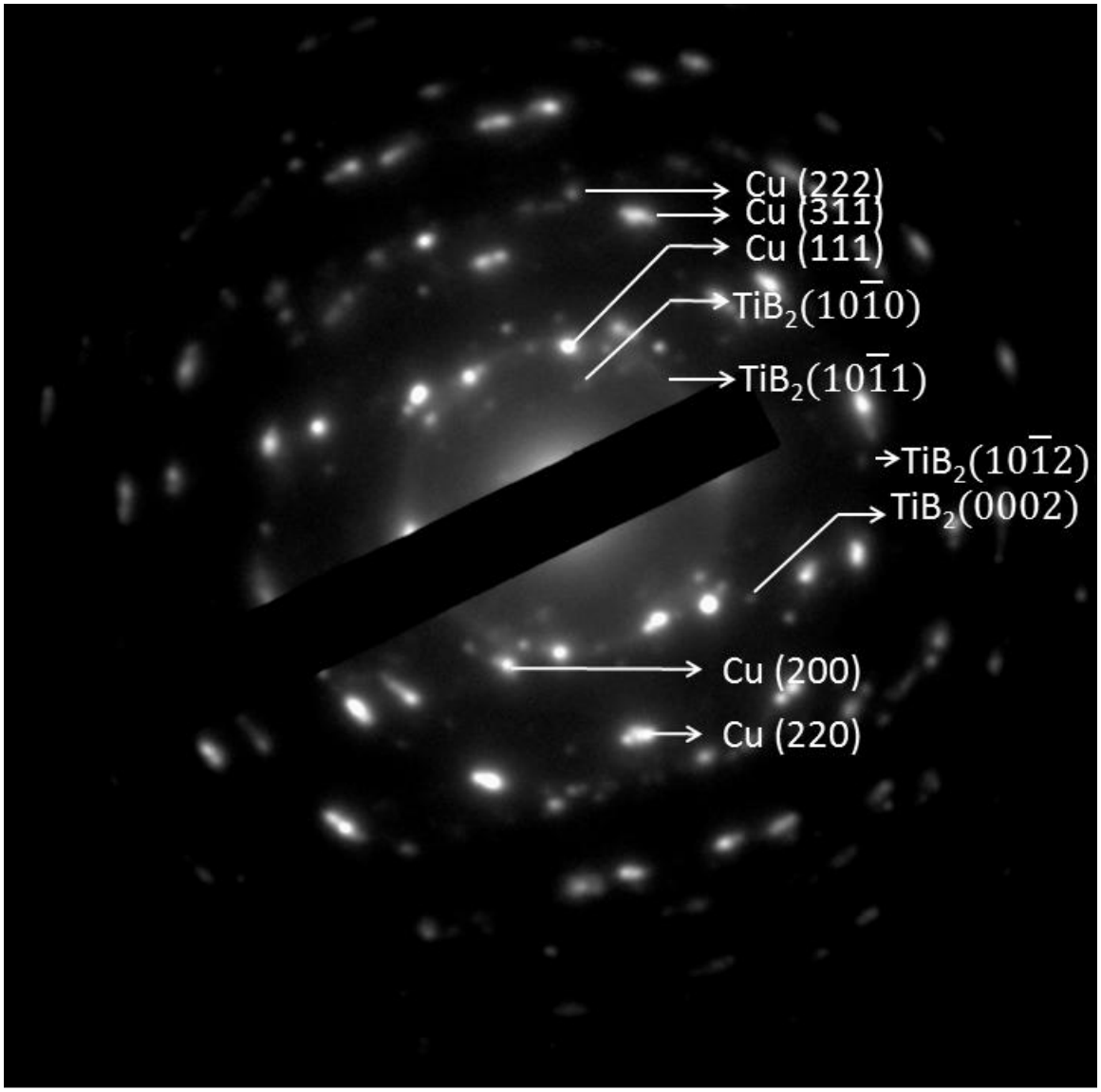

Figure 31. An electron diffraction pattern of a co-sputtered Cu-TiB_2 irradiated with a dose of 1×10^{16} ions/cm^{-2} Kr^{+} ions at 650 °C.

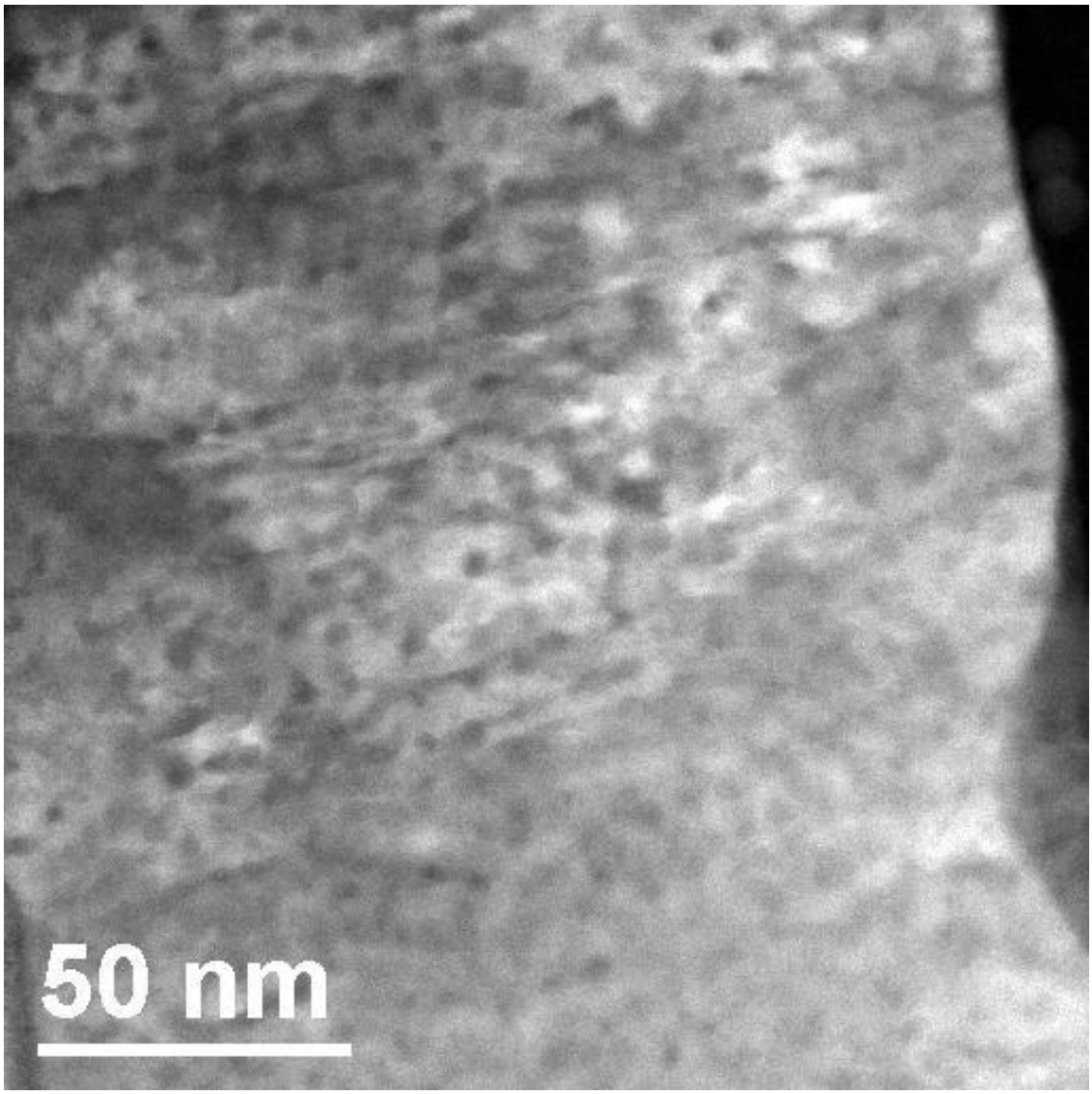

Figure 32. A HAADF image of the capped co-sputterd Cu-TiB_2 film irradiated at 650 °C, with an irradiation dose of 3×10^{16} ions/ cm^{-2}.

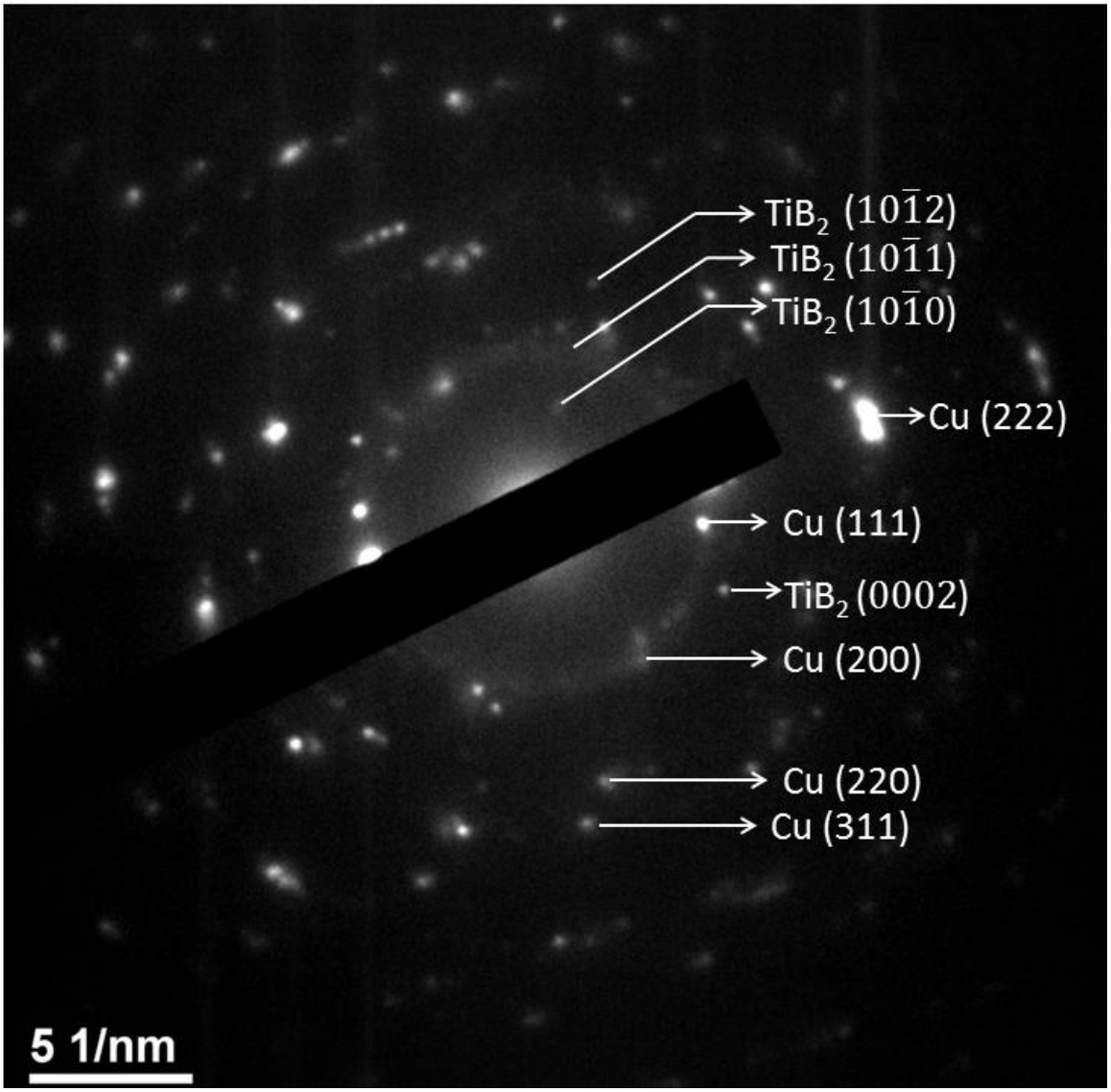

Figure 33. An electron diffraction pattern matching the extra reflections of TiB_2 in the capped co-sputtered $Cu_{0.85}(TiB_2)_{0.15}$ film irradiated at 650 °C with 3×10^{16} ions/ cm^{-2} Kr^{+} ions.

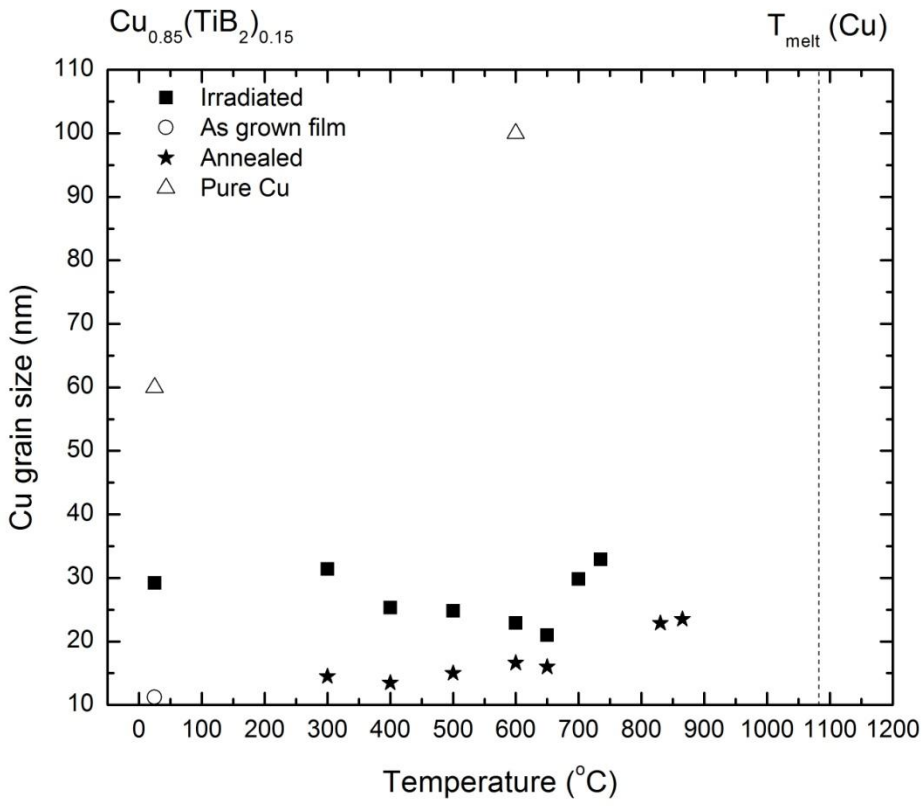

Figure 34. A plot of the Cu grain size vs temperature, comparing the grain size over different as grown, irradiated and annealed samples.

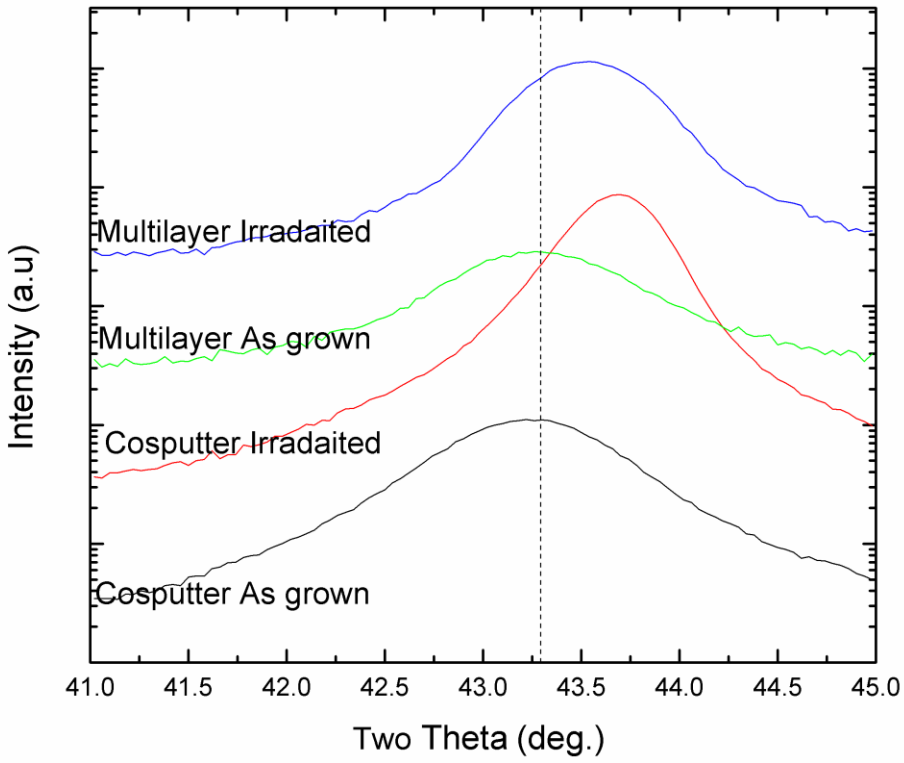

Figure 35. A comparison of as grown and irradiated samples in both co-sputtered film and multilayered film.